



OPEN Influence of operating pressure on the durability of a satellite hydraulic motor supplied by rapeseed oil

Pawel Sliwinski

This article describes the results of a durability test of a hydraulic satellite motor supplied by rapeseed oil. The tests were carried out on a test stand in a power recuperation system. The tests of the motor were carried out at a constant shaft speed for three fixed pressure drops in the motor. This made it possible to demonstrate the influence of the motor operating pressure on the durability of the satellite mechanism. The influence of the pressure drop in the motor and the influence of the operating time on the motor absorbency, on the torque on the motor shaft and the influence on the volumetric and hydraulic-mechanical efficiency are also shown. The basic relationship between the efficiency of the motor and the temperature rise in the motor is also described. The results of the calculations of the temperature rise in the motor are compared with the experimental results. The article also shows which components of the motor's working mechanism wear out the fastest. The cause of the wear and failure is also explained.

Keywords Hydraulic motor, Non-circular mechanism, Satellite mechanism, Energy efficiency, Oil, Life cycle, Discharge machining, Satellite, Rotor, Curvature

Hydraulic motors are executive organs in hydrostatic drive systems and their task is to convert hydraulic power into mechanical power^{1–6}. Various liquids can be used to power hydraulic motors. Nowadays, when we talk about hydraulic drive systems, the default is to think of mineral oil as the working liquid. However, there are also hydraulic systems in which other liquids are used, such as oil-in-water emulsions (HFA), synthetic liquids (HFD) and water. Other environmentally friendly liquids are also used, such as vegetable oils or, more generally, hydraulic oils developed on the basis of vegetable oils. The parameters of these liquids, such as viscosity, density, lubricating properties and liquid cleanliness, etc., influence the energy conversion efficiency of hydraulic systems and their durability^{7–17}.

In power hydraulics, vegetable oils are not yet as widely used as mineral oils. However, their properties have been systematically researched for some time in order to test the applicability of these oils as working liquids in hydrostatic systems^{18–22}. Among the vegetable oils, rapeseed oil is the most widely used. This oil stands out from other vegetable oils because of its easy availability on the market and its affordable price (it is lower than that of mineral oil).

Hydraulic oils based on vegetable oils with a viscosity class of VG46 are known on the market. These oils are enriched with thermo-oxidising, depressurising, anti-foaming and lubricating additives²⁰. They are therefore biodegradable vegetable oils with improved lubricating properties.

For over a dozen years now, developmental research has been carried out on a new generation of positive displacement hydraulic machines that can to work with different liquids, not only mineral oil, but also oil-in-water emulsion and pure water. These machines are satellite pumps and motors^{22–36}. The characteristics of satellite pumps and motors operating with these liquids (and especially water) have already been described in detail and published, e.g. in^{4,22,37–41}. Initial attempts were also made to test the properties of a satellite motor supplied with edible rapeseed oil (refined rapeseed oil). The first results are presented in^{41,42}. However, these publications contain no more information on the effects of the load M (torque) on the absorption Q , the volumetric efficiency η_v , and the pressure-mechanical efficiency η_{hm} as a function of the motor running time.

Faculty of Mechanical Engineering and Ship Technology (Division of Hydraulics and Pneumatics), Gdansk University of Technology, ul. Gabriela Narutowicza 11/12, 80-233 Gdańsk, Poland. email: pawel.sliwinski@pg.edu.pl

The literature on durability tests for other types of hydraulic motors is also sparse. In⁴³, for example, it was written that the wear of the surfaces of the rotor of hydraulic planetary motors increases the gaps, resulting in a reduction in speed of up to 65% and torque of up to 42%. And in⁴⁴, the change in the performance characteristics of the hydraulic planetary motor during operation was described for a certain range of changes in its operating parameters.

In order to obtain basic information on the durability of satellite motor supplied with liquids other than mineral oil, it was decided to carry out a further study on the durability of a hydraulic satellite motor supplied with edible rapeseed oil (refined rapeseed oil). It is generally known that this oil has poorer lubricating properties than mineral oil, but certainly better than water^{20–22,45}. This will give you information on how the efficiency of a motor changes depending on its operating time at nominal parameters and how long this motor will last (to the point of damage or destruction). The results of the material tests and the failure mechanisms of the satellite mechanism teeth, i.e. pitting and cracking at the tooth root, have already been described in the article⁴⁶.

The decision to test the hydraulic motor with edible vegetable oil was also made in order to assess its suitability and practicality for use in simple hydraulic systems operating indoors, i.e. at ambient temperatures above zero.

Tested motor

The research object was a prototype of a satellite hydraulic motor (Figs. 1 and 2). The operating principle of the satellite motor is generally known and is described in^{22,47–49}.

The motor uses satellite mechanism type 4×6 , i.e. the mechanism with a four-hump rotor ($n_R = 4$), a six-hump curvature ($n_E = 6$) and with ten satellites (Figs. 2 and 3). The theoretical working volume of the motor is $q_t = 16,7 \text{ cm}^3/\text{rev}$.

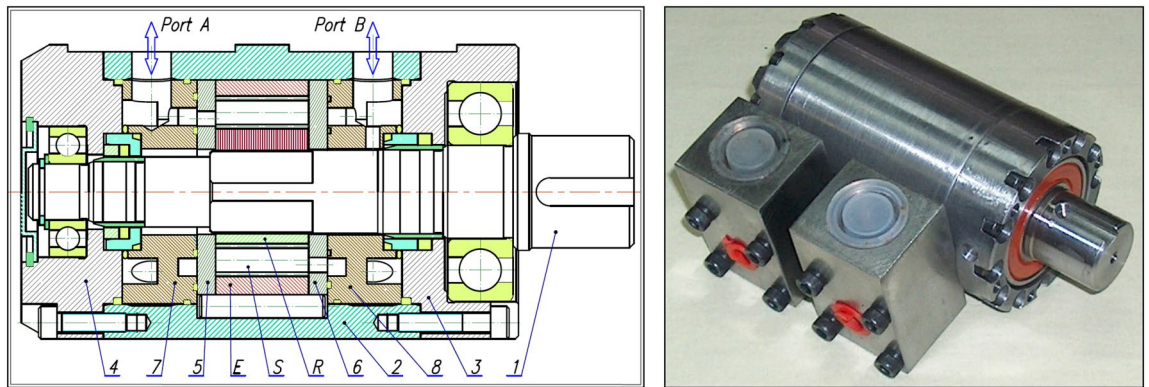


Figure 1. Tested motor (satellite motor)^{22,37,38,46–48}; E—external gear (curvature), S—satellite, R—rotor, 1—shaft, 2,3 and 4—housing, 5 and 6—commutation plates (compensation plates), 7 and 8—inflow/outflow manifolds.

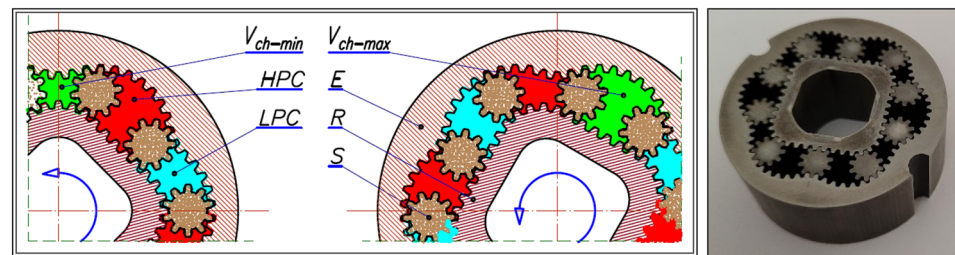


Figure 2. Satellite mechanism: E—external gear (curvature), R—rotor, S—satellite, HPC—high pressure chamber, LPC—low pressure chamber, V_{ch-min} —working chamber with minimum volume, V_{ch-max} —working chamber with maximum volume.

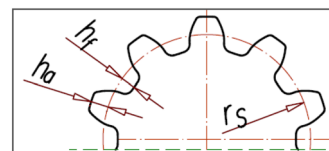


Figure 3. Basic parameters of the satellite: h_a —addendum, h_f —dedendum, r_s —the reference radius.

The publication³⁸ states that the considered mechanism is a scaled copy of the mechanism with module 1.5 mm. The mechanism with module 1.5 mm was designed so that it can be produced using classical machining methods (chiselling and milling). The pitch line of the rotor consists of circles with radii r_p and r_Q , which are connected at point T. The pitch line of the curvature was approximated by fragments of circles with radii r_{C1} and r_{C2} . A conceptual sketch of the rotor part of the satellite mechanism with the basic geometrical dimensions is shown in Fig. 4. The technical data of the satellite mechanism are listed in Table 1.

The non-core components of the satellite motor are the commutation plates (Fig. 1—items 5 and 6 and Fig. 5). They have the task of guiding the liquid into the working chambers of the motor and discharging it from them. Both plates are identical in design and manufacture.

The presented satellite mechanism was made of NIMAX steel (Table 2)⁵⁰. This mechanism was manufactured using the WEDM (Wire Electrical Discharge Machining) process. After the WEDM process, the mechanism was nitrided.

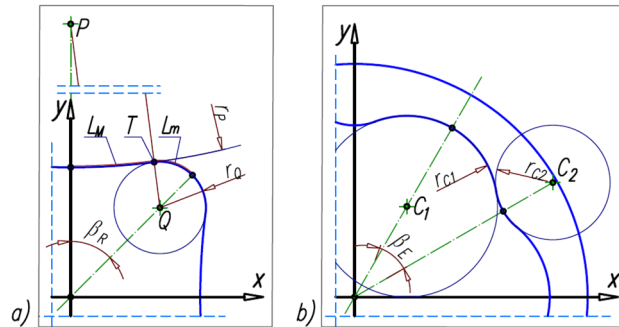


Figure 4. Geometry of the rotor of the tested satellite mechanism; r_{C1} and r_{C2} —radii of the circles of curvature, L_M —length of the arc with radius R_M , L_m —length of the arc with radius R_m , Technical data in Table 1.

| n_R | n_E | β_R | β_E | m | H |
|----------|-----------|-----------|-----------|-----------|------------|
| 4 | 6 | 45° | 30° | 0.6 mm | 20 mm |
| z_S | z_R | z_E | r_S | p_{bs} | α_p |
| 10 | 44 | 66 | 3.0 mm | 1.77 mm | 20° |
| r_P | x_P | y_P | r_Q | x_Q | y_Q |
| 202.2 mm | 0.0 mm | 213.78 mm | 6 mm | 5.657 mm | 5.657 mm |
| x_T | y_T | L_M | L_m | h_a | h_f |
| 6.895 mm | 11.130 mm | 5.508 mm | 4.859 mm | 0.26 mm | 0.21 mm |
| r_{C1} | x_{C1} | y_{C1} | r_{C2} | x_{C2} | y_{C2} |
| 9.333 mm | 5.380 mm | 9.319 mm | 5.898 mm | 20.333 mm | 11.739 |

Table 1. Parameters of the tested satellite mechanism³⁸. Symbols like in Figs. 3 and 4. Other symbols: H —nominal height of the satellite mechanism, m —the tooth module, z_E —the number of teeth on the external gear (curvature), z_R —the number of teeth on the rotor, z_S —the number of teeth on the satellite, α_p —the pressure angle, p_{bs} —the base pitch of the satellite teeth, $x_P, y_P, x_Q, y_Q, x_T, y_T, x_{C1}, y_{C1}, x_{C2}, y_{C2}$ —coordinates of points P, Q, T, C_1 and C_2 (Fig. 4).



Figure 5. Commutation (compensation) plate of the satellite motor.

| Density | Young module E | Poisson number ν | Surface hardness after gas nitriding |
|------------------------|----------------------------------|---------------------------------|--------------------------------------|
| 7900 kg/m ³ | 2.05 · 10 ¹¹ Pa | 0.3 | 950 MHV |
| Hardness | Yield strength R _{p0.2} | Tensile strength R _m | Depth after gas nitriding |
| ~ 370 HB | 785 MPa | 1265 MPa | 0.25 mm |

Table 2. Basic parameters of the NIMAX steel^{38,50}.

The article⁴⁶ describes material tests for the satellite mechanism. It was shown that the average case hardness of nitrided steel NIMAX is 1100 HV0.1 (with a range of 1080HV to 1180HV). The depth of the hardened insert was 0.4 mm. The teeth of the satellite mechanism are therefore hardened over their entire thickness.

During one full rotation of the rotor (360° rotation), the number n_{ch} of cycles volume change of all working chambers is as follows^{22,24,38}:

$$n_{ch} = n_E \cdot n_R \tag{1}$$

Publication³⁸ concluded that for one full revolution of the rotor, i.e. for $\alpha_R = 360^\circ$:

- (a) the number of contacts of each rotor tooth with the satellite tooth is $i_{RTS} = 6$;
- (b) the number of contacts of each curvature tooth with the satellite tooth is $i_{ETS} = 4$.

Based on the theoretical analyses, presented in the publication³⁸, it can also be concluded that the total number i_S of contacts satellite teeth with the rotor teeth and the curvature for one full revolution of the rotor (for $\alpha_R = 360^\circ$) is:

$$i_S = 0.2 \cdot z_E \cdot \frac{n_R}{n_E + n_R} \tag{2}$$

Thus, for the 4 × 6 type satellite mechanism $i_S = 5.28$. In addition, it was shown in³⁸ that for nitrided NIMAX steel, the contact fatigue strength of gears $\sigma_{Hlim} \approx 1250$ MPa, but the value of allowable normal stress in gears is maximally (in a very optimistic variant) $\sigma_{per} \approx 2500$ MPa. In³⁸ it was also shown that for $\Delta p_i = 25$ MPa the stresses in the teeth:

- (a) are not exceeded if the mechanism is backlash-free and therefore favourable values for the K and Z factors are assumed in the stress calculation formulae;
- (b) are exceeded by up to 60% (assuming unfavourable values for the K and Z factors in the calculations).

Working liquid

Refined rapeseed oil (edible oil) was used as the working liquid in the system. The characteristics of dynamic viscosity μ and density ρ of this oil are shown in Figs. 6 and 7. For comparison, the viscosity μ and density ρ characteristics of the mineral oil Total Azolla ZS 46 are also shown in these figures. It is clear that the density ρ of the oil decreases with increasing temperature t . The density ρ of rapeseed oil can be described by the following empirical formula (Fig. 7):

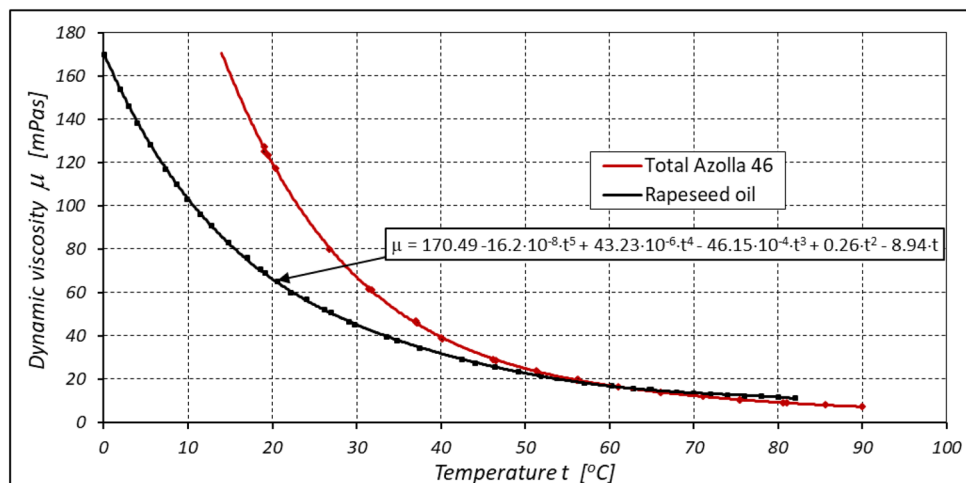


Figure 6. Dynamic viscosity μ of refined rapeseed oil (edible oil) and Total Azolla 46 mineral oil.

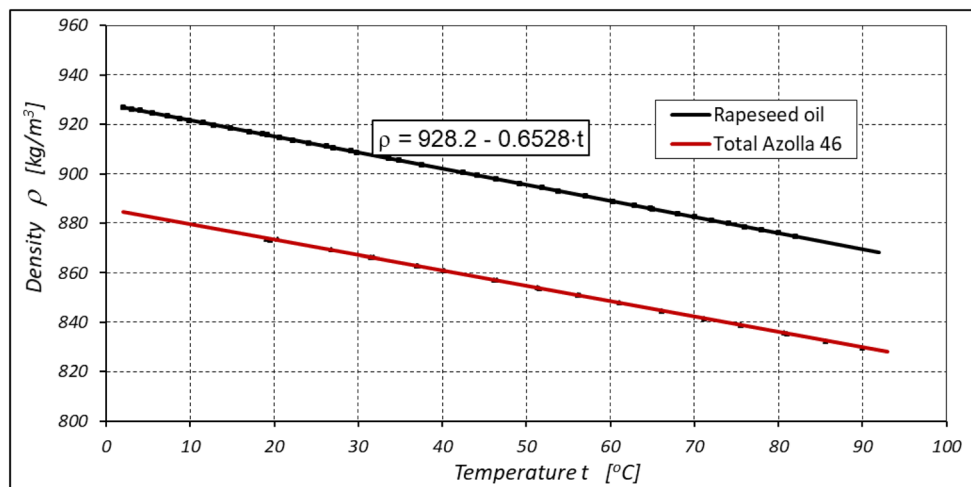


Figure 7. Density ρ of refined rapeseed oil (edible oil) and Total Azolla 46 mineral oil.

$$\rho = 928.2 - 0.653 \cdot t \left[\frac{\text{kg}}{\text{m}^3} \right] \quad (3)$$

However, the specific heat c of rapeseed oil is somewhat lower than the specific heat of mineral oil. For rapeseed oil $c = 1850 \frac{\text{J}}{\text{kg} \cdot \text{K}}$, but for mineral oil $c = 1880 \frac{\text{J}}{\text{kg} \cdot \text{K}}$ (for comparison, the specific heat of water $c = 4180 \frac{\text{J}}{\text{kg} \cdot \text{K}}$ ⁵¹).

The results of the lubricating properties test described in^{22,45} show that the limit seizure pressure p_{oz} for refined rapeseed oil is $p_{oz} = 287.5$ MPa and for mineral oil Total Azolla ZS 46 is $p_{oz} = 386.4$ MPa. Rapeseed oil therefore has poorer lubricating properties than mineral oil. The difference in the seizure pressure limit values is up to 25%^{22,45}.

Test rig

The durability test of the satellite motor was carried out on the test rig shown in Figs. 8 and 9. This test rig is equipped with an energy recovery and has been presented in many publications, including^{37,39,40,47–49}. It should be made clear at this point that the hydraulic system of the test rig was cleaned and flushed before the tests. The tank was filled with 500 L of rapeseed oil.

The following parameters were measured during the motor test:

- pressure p_1 in the inlet port (strain gauge pressure transducer, range $0 \div 25$ MPa, class 0.3);
- pressure p_2 in the exhaust port (strain gauge pressure transducer, range $0 \div 2.5$ MPa, class 0.3);
- motor absorbency Q (mass flowmeter, range $0 \div 33$ l/min, class 0.1);

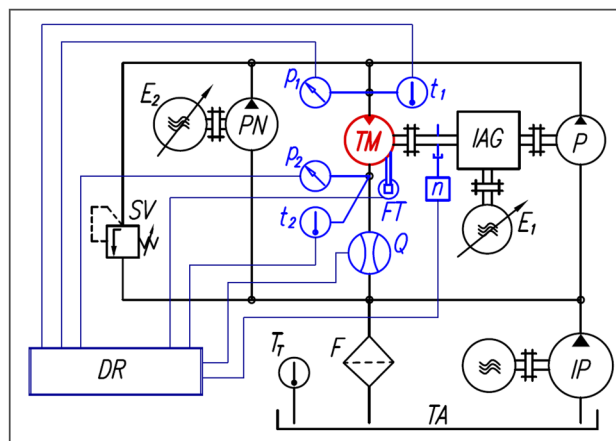


Figure 8. The hydraulic and measuring system of the test rig: P—pump, TM—tested motor, PN—pump for filling leaks in P and M, IP—impeller pump, SV—safety valve, F—filter, TA—tank, IAG—intersecting axis gear, E_1 and E_2 —electric motors with frequency converters, DR—data recorder, p_1 , p_2 —pressure transducers, t_1 , t_2 , t_1 —temperature transducers, Q—flowmeter, FT—force transducer for torque M measurement, n—inductive sensor for rotational speed measurement,

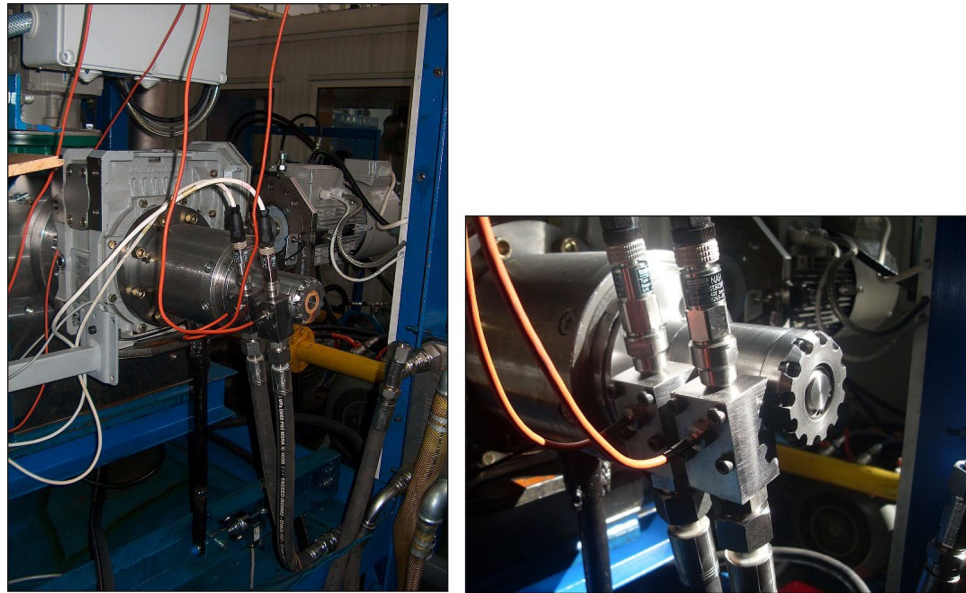


Figure 9. View of part of the test rig (left) with the satellite motor mounted for the test (right).

- torque M (strain gauge force transducer FT mounted on the arm 0.5 m (the arm is fixed to the motor body), range $0 \div 100$ N, class 0.1);
- rotational speed n of the motor shaft (inductive sensor, accuracy of measurement ± 0.01 rpm);
- temperatures t_1 and t_2 of liquid in the inlet and exhaust ports of the motor (RTD temperature sensor, class A, max. error 0.5 °C).

On the test rig mentioned above, it is very easy to keep the constant pressure drop Δp measured in the motor ports (by adjusting the pump speed PN and thus its capacity accordingly—Fig. 8). This pressure drop is:

$$\Delta p = p_1 - p_2 \quad (4)$$

If $\Delta p = \text{const.}$ then torque M , measured at the motor shaft, is⁴⁰:

$$M = \frac{q_t \cdot \Delta p_i}{2 \cdot \pi} - M_L \quad (5)$$

where: q_t —the theoretical working volume of the motor, M_L —the torque of the mechanical losses, Δp_i —the pressure drop in the working chambers of the motor⁴⁹: $\Delta p_i = \Delta p - \Delta p_{ich}$ (6), Δp_{ich} —the pressure drop in the internal channels of the motor.

The method for determining Δp_{ich} is described in detail in⁴⁹. Thus, the pressure drop Δp_i that load the working mechanism is smaller than the pressure drop Δp measured in the motor ports. In this way Δp_i influences the wear of the working mechanism.

Relationship between the efficiency of the motor and the temperature rise in the motor

Every positive displacement machine (pump or motor) is characterised by energy losses. The amount of power N_L lost in the motor is calculated as follows:

$$N_L = Q \cdot \Delta p - \frac{\pi}{30} \cdot M \cdot n \quad (7)$$

where: Q —the motor absorbency, n —rotational speed of the motor shaft.

The power N_L lost in the hydraulic motor influences the temperature rise of the motor components and the temperature rise Δt of the liquid in the motor ports. The heat flow from the liquid to the surroundings through the motor components is very low compared to the heat flow in the liquid. Therefore, the heat flow from the liquid to the surroundings is ignored in the considerations and it is assumed that the entire power lost N_L is absorbed by the liquid⁵². It can therefore be written that:

$$N_L = \rho \cdot Q \cdot c \cdot \Delta t_\mu \quad (8)$$

where: Δt_μ —the temperature rise of the liquid due to energy losses (depending on the viscosity μ of the liquid), c —the specific heat of the oil, ρ —the density of the oil.

In addition to the temperature rise Δt_μ of the liquid, there is a temperature drop Δt_{ai} which is associated with the pressure drop Δp of the liquid in the motor and is calculated as follows⁵²:

$$\Delta t_{ai} = k \cdot \Delta p \quad (9)$$

where k is the constant that depend on the initial temperature of the liquid. For mineral oil at $t_1 = 40 \div 50 \text{ }^\circ\text{C}$ $k = 0.128 \text{ }^\circ\text{C}/\text{MPa}$ can be assumed⁵². The value of the constant k for rapeseed oil is not known and will be the subject of further analyses.

The temperature rise Δt in the motor ports is therefore:

$$\Delta t = \Delta t_\mu - \Delta t_{ai} \quad (10)$$

A comparison of formulae (7) and (8) shows that:

$$\Delta t_\mu = \frac{1}{\rho \cdot c} \cdot \left(\Delta p - \frac{\pi}{30} \cdot M \cdot \frac{n}{Q} \right) \quad (11)$$

Considering that the total efficiency η_c of a motor is defined as:

$$\eta_c = \frac{\pi}{30} \cdot \frac{M}{\Delta p} \cdot \frac{n}{Q} = \eta_v \cdot \eta_{hm} \quad (12)$$

then:

$$\Delta t_\mu = \frac{\Delta p}{\rho \cdot c} \cdot (1 - \eta_v \cdot \eta_{hm}) \quad (13)$$

where: η_v —the volumetric efficiency of the motor; η_{hm} —the pressure-mechanical efficiency of the motor.

Substituting formula (9) and (13) into formula (10) finally results in the following formula:

$$\Delta t = \Delta p \cdot \left(\frac{1}{\rho \cdot c} \cdot (1 - \eta_v \cdot \eta_{hm}) - k \right) \quad (14)$$

It can be seen from this that if the efficiency η_c of the motor decreases, the temperature rise Δt in the motor is greater. If the value of the constant k is not known, it can be determined by transforming Eq. (13), namely:

$$k = \frac{1}{\rho \cdot c} \cdot (1 - \eta_v \cdot \eta_{hm}) - \frac{\Delta t}{\Delta p} \quad (15)$$

The values of Δt , Δp , η_v and η_{hm} in the above formula were determined from experimental data. However, it is known that the efficiencies η_v and η_{hm} depend on the pressure drop Δp in the motor^{39,40,49}. In order to obtain a more reliable result, it is therefore proposed to calculate the constant k as:

$$k = \frac{1}{n} \cdot \sum_{i=1}^n k_{(i)} \quad (16)$$

where: $k_{(i)}$ —the value of constant k calculated according to formula (15) for the i -th pressure drop Δp in the motor; n —the number of values of Δp and thus the number of calculated values of the constant $k_{(i)}$.

Conditions for conducting the experiment

Three series of durability tests of the satellite motor were performed. A new working mechanism was maintained was used in each series of tests. In each series of tests, a constant pressure drop Δp was maintained in the motor, i.e.:

- (1) the first series—at $\Delta p = 20 \pm 0.5 \text{ MPa}$;
- (2) the second series—at $\Delta p = 15 \pm 0.5 \text{ MPa}$;
- (3) the third series—at $\Delta p = 10 \pm 0.5 \text{ MPa}$.

The motor tests were carried out at the one constant speed $n = 1500 \pm 1 \text{ rpm}$ (in all three series).

The liquid temperature was not stabilised in the test rig, as can be seen in detail from the temperature characteristics in the following sections. When, the system was started, the temperature was therefore significantly lower than during the test. In this way, the actual operating conditions of the motor in the industrial equipment were reflected.

Before the new satellite mechanism was installed to the motor, the heights of the mechanism's components were measured at the MP points as shown in Figs. 10 and 11. The mass of these elements was also measured. The height H_E of the curvature is the average value of the measurements at the six points. Similarly, the height H_R of the rotor was calculated (as the average of four measurements).

The axial clearance h_R of the rotor was calculated as:

$$h_R = H_E - H_R \quad (17)$$

and the axial clearance h_s of the satellites was calculated as:



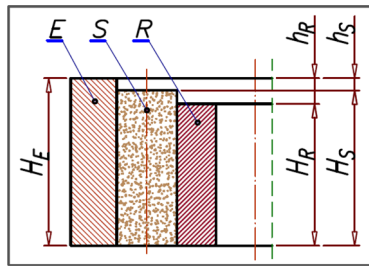


Figure 10. The height H_E of the curvature, the axial clearance h_S of the satellite, the axial clearance h_R of the rotor.

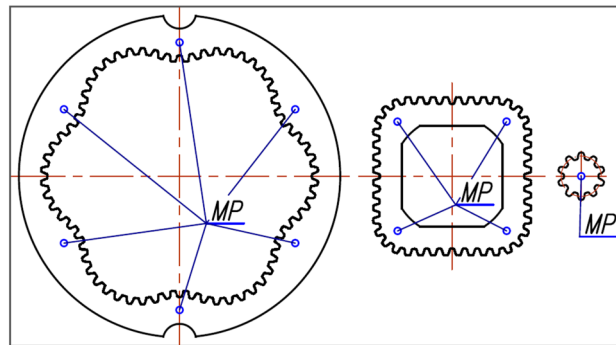


Figure 11. Points MP for measuring the height H_E of the curvature, the height H_R of the rotor and the height H_S of the satellite.

$$h_S = H_E - \frac{\sum_{i=1}^{i=n_R+n_E} H_{Si}}{n_S} \tag{18}$$

where: H_E —the height of the curvature, H_R —the height of the rotor. H_{Si} —the height of the i -th satellite. n_S —the number of satellites.

The values for the height of the components of the mechanism, their masses and the values of the axial clearance of the rotor and the satellites are presented in the next section.

In each series, the tests were carried out in an intermittent cycle, i.e. the test stand was switched off from time to time. The test stand was also switched off at the end of the working day. The interruption of the test is represented by a vertical orange dashed line in each test drawing (in the following section). In addition, the motor was disassembled from time to time, the mechanism was cleaned, wear products were removed and the heights of the mechanism components and their weights were measured. The removal of wear products from the surfaces of the mechanism components required lapping of these surfaces. At the same time, they were lapped so as not to reduce the original height of these components. The values h_R and h_S were calculated according to the formulae (17) and (18). In each figure showing the results of the study (figures in the following section), the time at which the disassembly was performed is illustrated with a vertical blue dashed line.

In order to objectively compare the wear, the relative weight loss of the components was calculated using the following formula:

$$\delta m_S = 100 \cdot \left(1 - \frac{\sum_{i=1}^{i=n_S} m_{Si}}{\sum_{i=1}^{i=n_S} m_{Si(t=0)}} \right) \tag{19}$$

$$\delta m_E = 100 \cdot \left(1 - \frac{m_E}{m_{E(t=0)}} \right) \tag{20}$$

$$\delta m_R = 100 \cdot \left(1 - \frac{m_R}{m_{R(t=0)}} \right) \tag{21}$$

where: $m_{Si(t=0)}$, $m_{R(t=0)}$, $m_{E(t=0)}$ —the initial mass of the satellite, the rotor and the curvature (for $t = 0$ min.); m_{Si} , m_R , m_E —the mass of the satellite, the rotor and the curvature during the test.

The experimental data corresponding to the set-up time τ_s , i.e. the time to start and stop the hydraulic and measurement system, the time to set the parameters, etc., are not shown in the test results (tables and figures).

During this time the motor was operated at a speed in the range of $0 \div 1500$ rpm and in the pressure drop range Δp corresponding to the each series of measurements, i.e. $\Delta p = 20, 15$ and 10 MPa respectively. It was estimated that the time of unstabilised motor operation was:

- (1) in the first series (at $\Delta p = 20$ MPa)—about 40 min;
- (2) in the second series (at $\Delta p = 15$ MPa)—about 30 min;
- (3) w trzeciej serii (dla at $\Delta p = 10$ MPa)—about 52 min.

and his mean rotational speed is about $n_m = 750$ rpm.

Results of the tests

Results of the test at $\Delta p = 20$ MPa

Table 3 shows the mass of the components of the satellite mechanism, the height H_E of the curvature and the average values h_R of the axial clearances of the rotor and the average values h_S of the axial clearances of the satellites measured before, during and after the tests.

The results of measurements of the pressures p_1 and p_2 , the absorption Q , the torque M and the temperatures t_1 and t_2 in the motor ports are shown in Figs. 12, 13, 14 and 15.

After 2135 min of operation, the satellite mechanism was destroyed (Fig. 16).

Photographs of the satellite mechanism components during and after the test are shown in Figs. 17, 18 and 19.

Results of the test at $\Delta p = 15$ MPa

Table 4 shows the mass of the components of the satellite mechanism, the height H_E of the curvature and the average values h_R of the axial clearances of the rotor and the average values h_S of the axial clearances of the satellite measured before, during and after the tests.

The results of the measurements of the pressures p_1 and p_2 , the absorption Q , the torque M and the temperatures t_1 and t_2 at the motor ports are shown in Figs. 20, 21, 22 and 23.

After 3092.55 min of operation, the satellite mechanism was destroyed. The process of wear of the mechanism components until failure was similar to the tests for $\Delta p = 20$ MPa (Figs. 17, 18 and 19).

| | | m_E (g) | m_R (g) | m_S [g] | H_E (mm) | h_R (μm) | h_S (μm) |
|-------------------|------|-----------|-----------|-----------|------------|-------------------------|-------------------------|
| Time τ (min) | 0 | 99.813 | 43.104 | 4.536 | 19.998 | 4.5 | 6.2 |
| | 11.5 | 99.801 | 43.103 | 4.535 | 20.007 | 6.5 | 6.45 |
| | 229 | 99.788 | 43.075 | 4.533 | 20.009 | 7.0 | 7.1 |
| | 765 | 99.781 | 43.010 | 4.529 | 20.011 | 7.0 | 9.1 |
| | 1677 | 99.741 | 42.745 | 4.521 | 20.010 | 7.5 | 8.35 |
| | 2135 | 99.726 | damage | 4.516* | 20.019 | damage | 7.75* |

Table 3. Mass, height and clearances of the components of the satellite mechanism—test for $\Delta p = 20$ MPa. Symbols H_E , h_R and h_S like in Fig. 10. m_S —the average mass of the satellites, m_E —the mass of the curvature, m_R —the mass of the rotor. *Measurement for only four satellites (6 were broken).

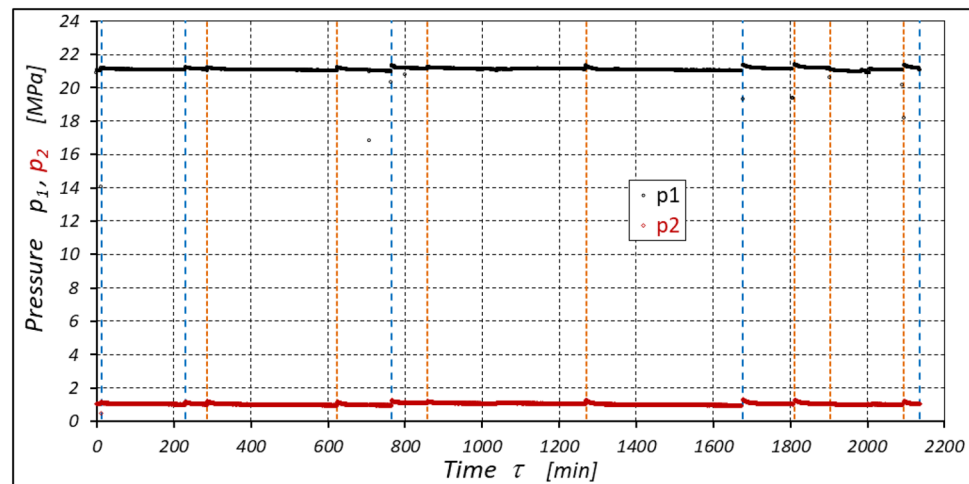


Figure 12. Characteristics of the pressure p_1 and p_2 in the motor ports as a function of time τ for $\Delta p = 20$ MPa and $n = 1500$ rpm.

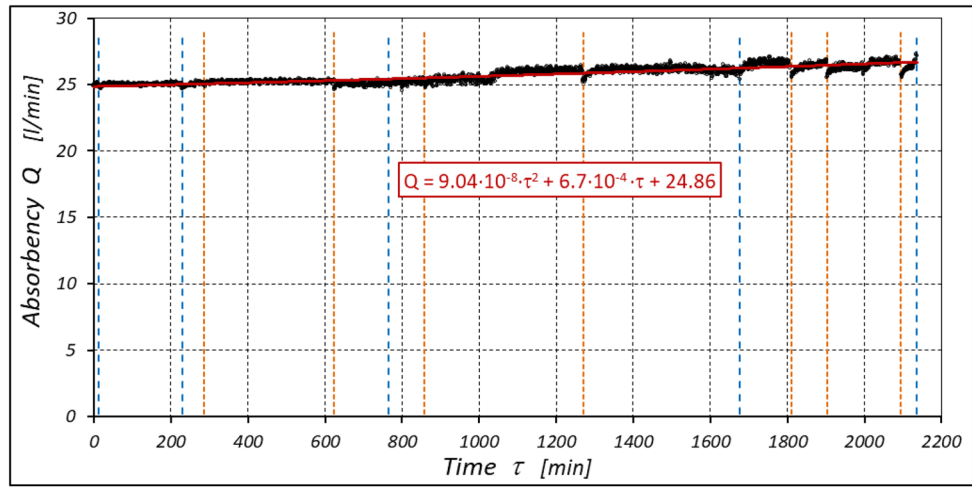


Figure 13. Characteristics of the motor absorbency Q as a function of time τ for $\Delta p = 20$ MPa and $n = 1500$ rpm.

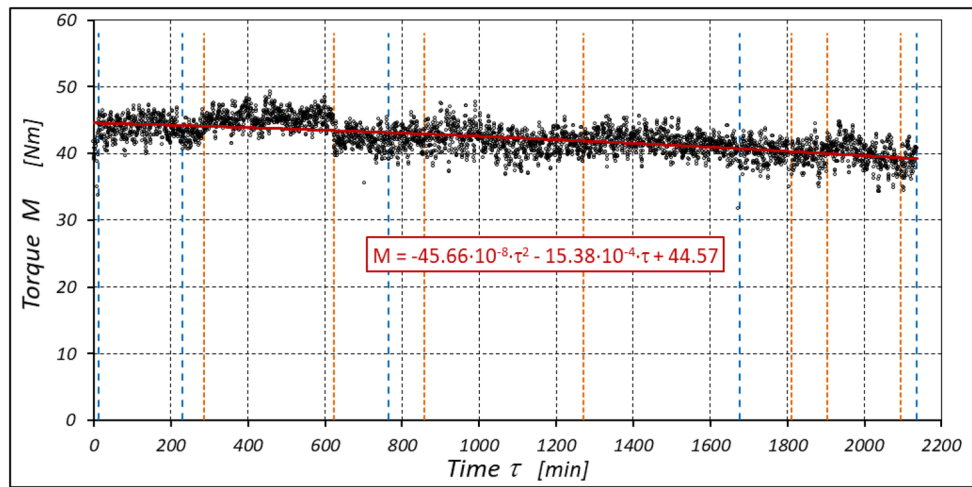


Figure 14. Characteristics of the torque M as a function of time τ for $\Delta p = 20$ MPa and $n = 1500$ rpm.

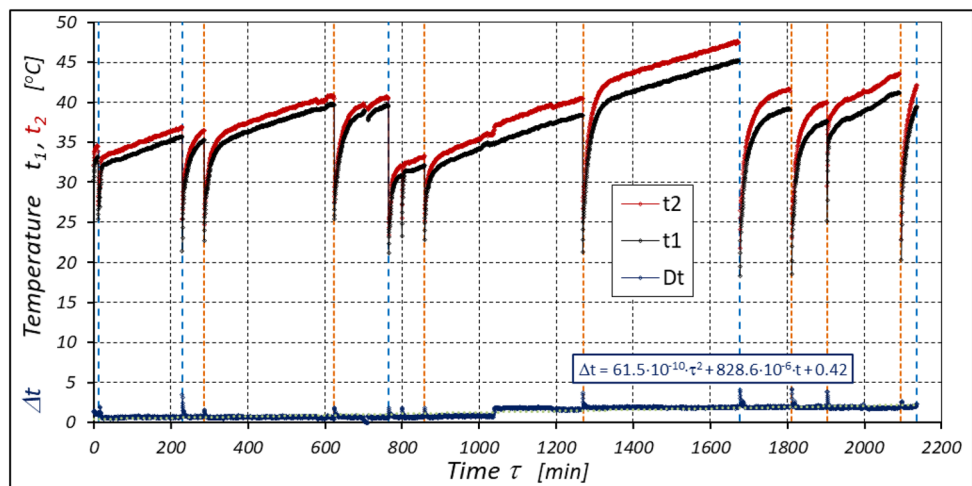


Figure 15. Characteristics of the temperatures t_1 and t_2 in the motor ports as a function of time τ for $\Delta p = 20$ MPa and $n = 1500$ rpm.



Figure 16. The destroyed satellite mechanism.



Figure 17. Fretting on the commutation plate: (a) after 11.5 min of operation; (b) after 1667 min of operation, (c) after completion of the test.

Results of the test at $\Delta p = 10$ MPa

Table 5 shows the mass of the components of the satellite mechanism, the height H_E of the curvature and the average values h_R of the axial clearances of the rotor and the average values h_S of the axial clearances of the satellite measured before, during and after the tests.

The results of the measurements of the pressures p_1 and p_2 , the absorption Q , the torque M and the temperatures t_1 and t_2 at the motor ports are shown in Figs. 24, 25, 26 and 27.

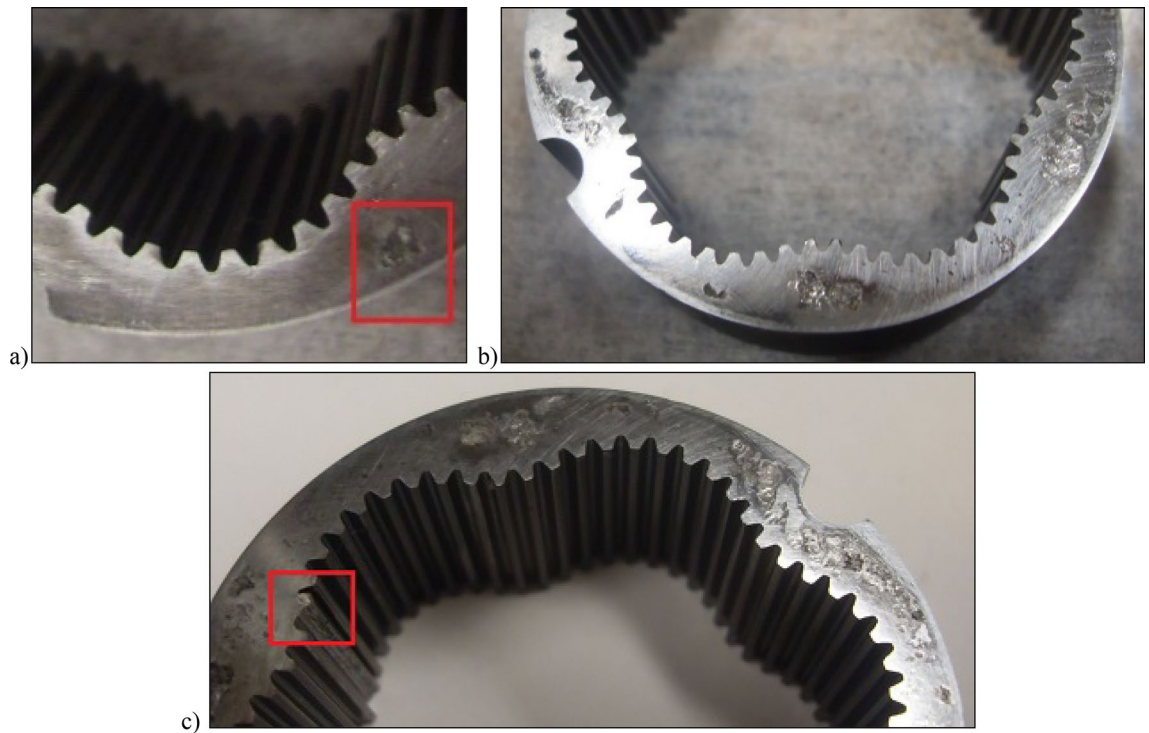


Figure 18. Fretting on the curvature: (a) after 11.5 min of operation; (b) after 1667 min of operation, (c) after completion of the test.

After more than 110 h (6652 min – Table 5) of testing, the motor was disassembled and no damage to the components of the mechanism visible to the naked eye was found (Fig. 28). Only an increase in satellite clearances in the mechanism and pitting on the curvature and on the commutation plates were visible. The test of the motor was terminated at this stage.

The publication⁴² states that during the first tests of the satellite motor supplied with rapeseed oil, a phenomenon was observed, namely a black ring on the face of the rotor and a purple ring on the commutation plate at the point of interaction with the rotor. This was also the case here, i.e. during tests at $\Delta p = 10$ MPa. After each disassembly of the satellite mechanism, both the black ring on the rotor surface and the purple ring on the commutation plate were also observed (Fig. 29). It was found that the thickness of the ring on the rotor is close to the height of the gap between the rotor and the commutation plate.

It is significant that these rings were not present when testing the motor with higher pressure drop, i.e. at $\Delta p = 15$ MPa and at $\Delta p = 20$ MPa.

Discussion

The test results have shown that in the first minutes of the motor operation (the non-worn mechanisms):

- the absorption Q of the motor is largest (24.9 l/min) for the highest pressure drop in the motor ($\Delta p = 20$ MPa) and smallest (24.4 l/min) for the lowest pressure drop ($\Delta p = 10$ MPa) (Fig. 30). This is consistent with the flow theory for hydraulic motor described in³⁹;
- similarly, the torque M on the motor shaft is the highest (44.6 Nm) for the highest pressure drop in the motor ($\Delta p = 20$ MPa) and lowest (19.2 Nm) for the lowest pressure drop ($\Delta p = 10$ MPa) (Fig. 31). This agrees with the theory that describes the influence of the load (torque) M on the pressure drop Δp in the motor, as described in⁴⁰ and shown in formulae (5) and (6).

With the hydraulic motor operation time τ (at $n = \text{const.}$), the motor absorbency Q increases and the torque M decreases (Figs. 30 and 31). The greatest increase in absorbency Q is observed for the most heavily loaded motor (Fig. 30). Therefore, an increase in absorbency means a lower volumetric efficiency η_v of the motor (Fig. 32). The increase in the absorbency Q of the motor also means an increase in the pressure drop Δp_{ich} in the internal channels of this motor, which in turn, at $\Delta p = \text{const.}$, causes a smaller pressure drop Δp_i in the working chambers, i.e. $\Delta p_i < \Delta p$ (according to formula (6)). For absorbency $Q = 24.4 \div 24.9$ l/min is $\Delta p_{\text{ich}} \approx 1.4$ MPa (determined according to the method described in⁴⁹). So, according to formula (6) the following pressure difference occurs in the chambers of the working mechanism:

- (a) $\Delta p_i \approx 18.6$ MPa for $\Delta p = 20$ MPa;

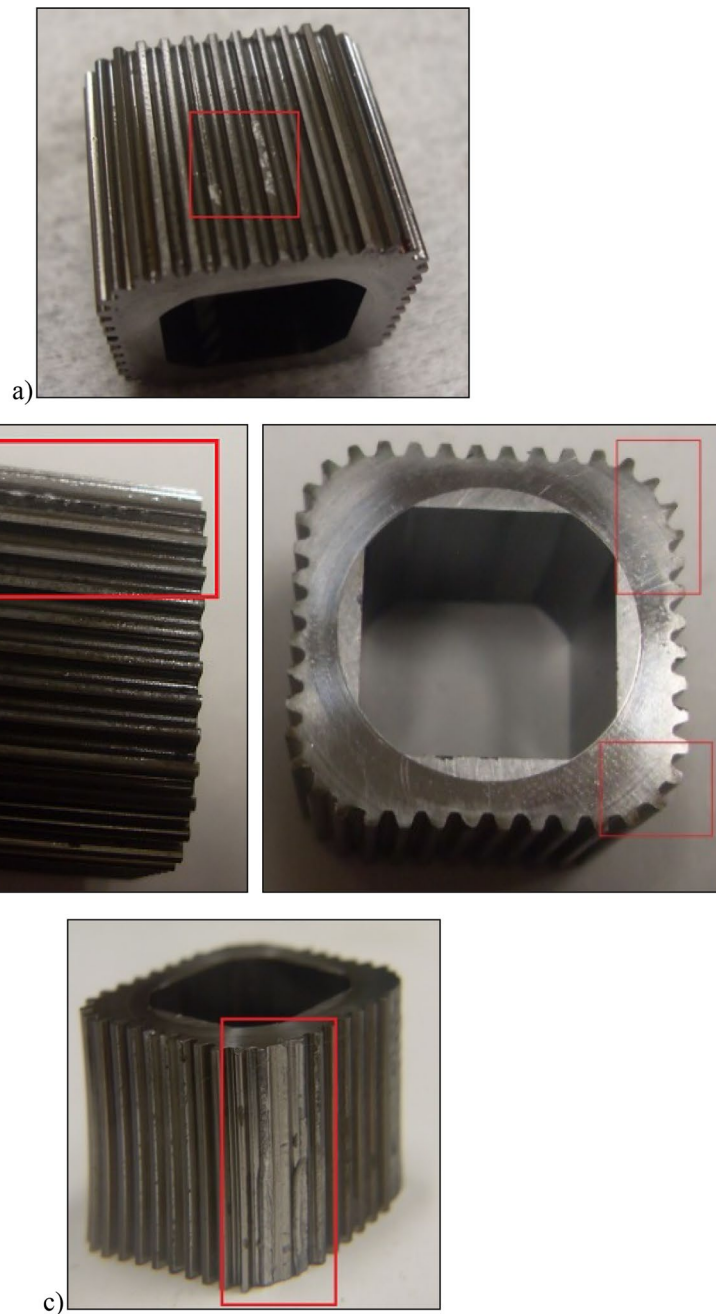


Figure 19. Photos of the rotor: (a) after 765 min of operation; (b) after 1667 min of operation, (c) after completion of the test.

| | | m_E (g) | m_R (g) | m_S (g) | H_E (mm) | h_R (μm) | h_S (μm) |
|-------------------|--------|-----------|-----------|-----------|------------|-------------------------|-------------------------|
| Time τ (min) | 0 | 99.849 | 43.168 | 4.536 | 20.002 | 5.15 | 4.50 |
| | 550 | 99.832 | 43.139 | 4.532 | 20.008 | 7.21 | 8.15 |
| | 1415 | 99.804 | 43.095 | 4.526 | 20.010 | 10.18 | 8.86 |
| | 2690 | 99.738 | 43.007 | 4.518 | 20.013 | 11.02 | 9.03 |
| | 3092.5 | 99.829 | 42.985 | 4.526 | 20.014 | 12.00 | 9.00 |

Table 4. Mass, height and clearances of the components of the satellite mechanism—test for $\Delta p = 15$ MPa. Symbols H_E , h_R and h_S like in Fig. 10.

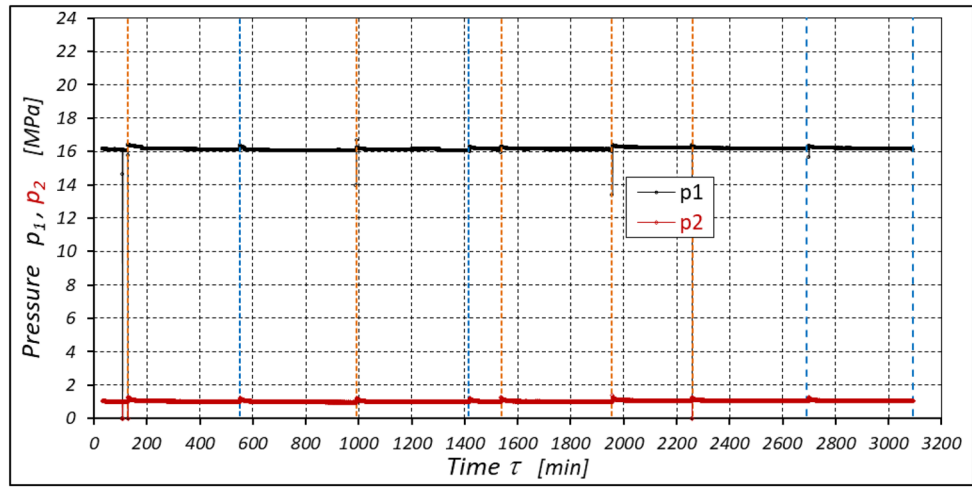


Figure 20. Characteristics of the pressure p_1 and p_2 in the motor ports as a function of time τ for $\Delta p = 15$ MPa and $n = 1500$ rpm.

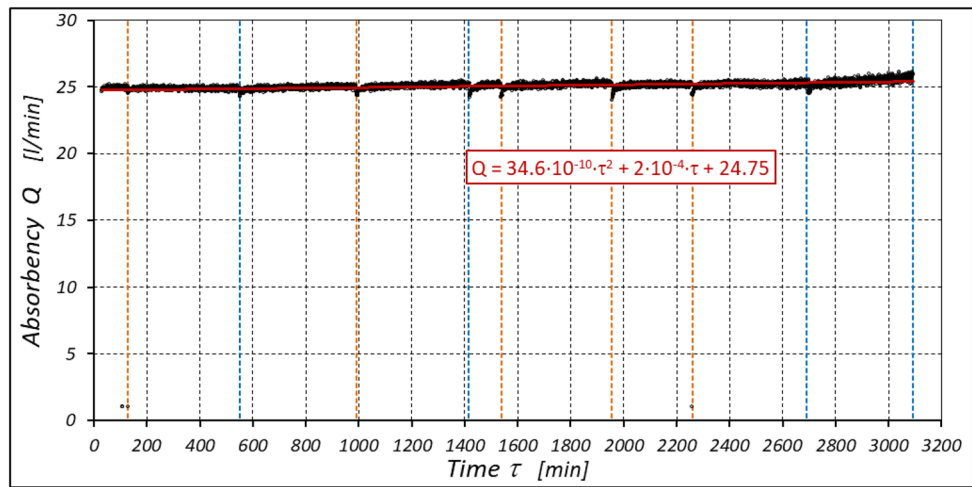


Figure 21. Characteristics of the motor absorbency Q as a function of time τ for $\Delta p = 15$ MPa and $n = 1500$ rpm.

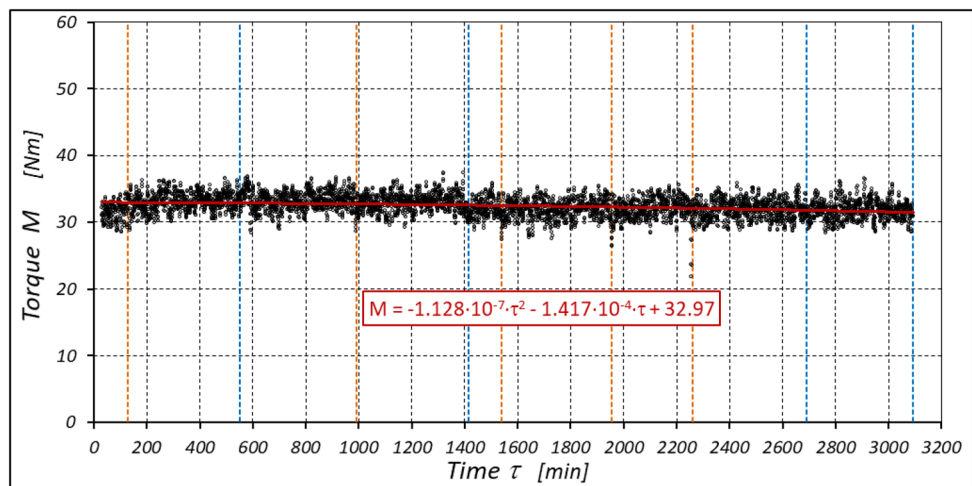


Figure 22. Characteristics of the torque M as a function of time τ for $\Delta p = 15$ MPa and $n = 1500$ rpm.

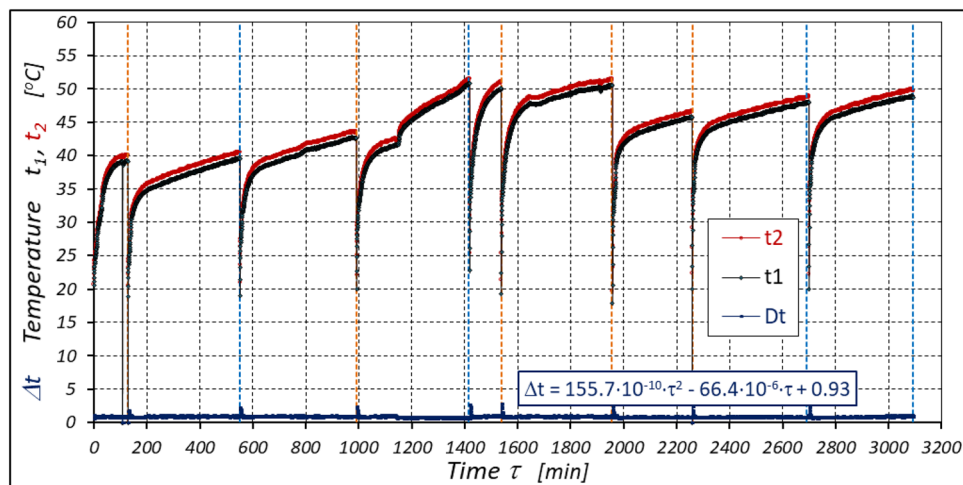


Figure 23. Characteristics of the temperatures t_1 and t_2 in the motor ports as a function of time τ for $\Delta p = 15$ MPa and $n = 1500$ rpm.

| | | m_E (g) | m_R (g) | m_S (g) | H_E (mm) | h_R (μm) | h_S (μm) |
|-------------------|-------|-----------|-----------|-----------|------------|-------------------------|-------------------------|
| Time τ (min) | 0 | 99.650 | 43.054 | 4.532 | 19.895 | 5.5 | 5.8 |
| | 1408 | 99.610 | 43.005 | 4.522 | 19.902 | 6.1 | 6.1 |
| | 1814 | 99.591 | 42.940 | 4.520 | 19.923 | 30.5 | 32.15 |
| | 3237 | 99.532 | 42.896 | 4.511 | 19.922 | 29.0 | 32.4 |
| | 4797 | 99.423 | 42.809 | 4.495 | 19.934 | 39.5 | 41.6 |
| | 6652* | 99.315 | 42.715 | 4.473 | 19.930 | 39.0 | 40.5 |

Table 5. Mass, height and clearances of the components of the satellite mechanism—test for $\Delta p = 10$ MPa. Symbols H_E , h_R and h_S like in Fig. 10. *The mechanism is not broken!

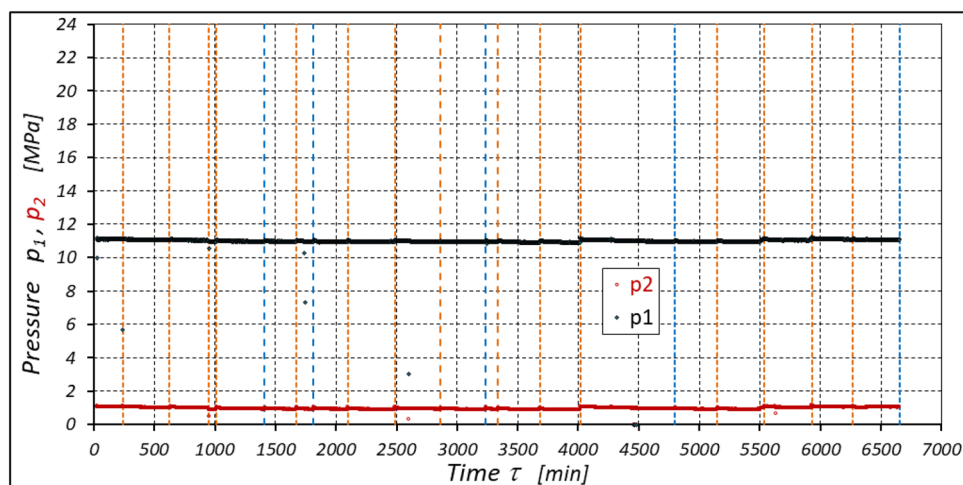


Figure 24. Characteristics of the pressure p_1 and p_2 in the motor ports as a function of time τ for $\Delta p = 10$ MPa and $n = 1500$ rpm.

- (b) $\Delta p_i \approx 13.6$ MPa for $\Delta p = 15$ MPa;
- (c) $\Delta p_i \approx 8.6$ MPa for $\Delta p = 10$ MPa.

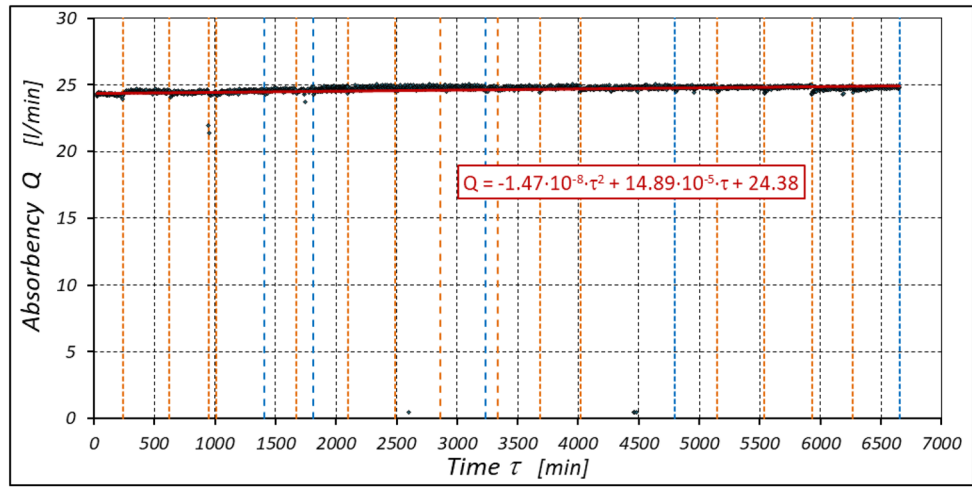


Figure 25. Characteristics of the motor absorbency Q as a function of time τ for $\Delta p = 10$ MPa and $n = 1500$ rpm.

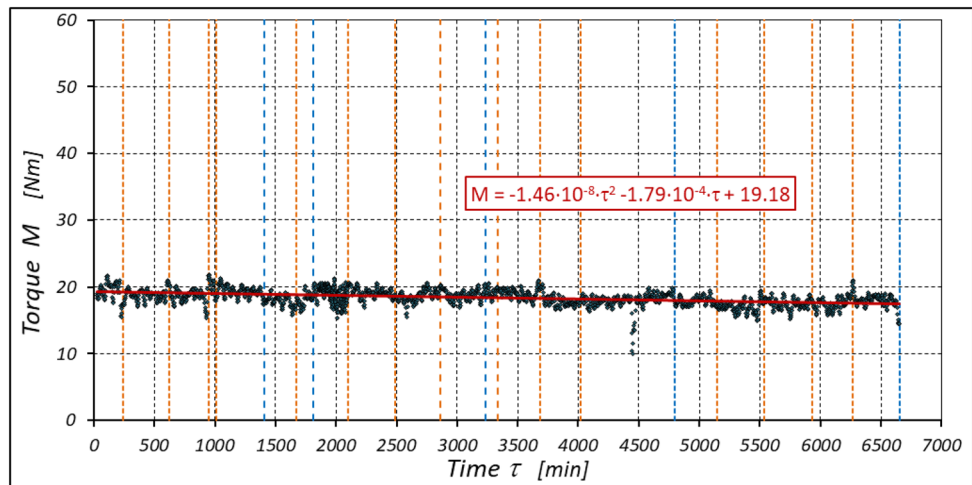


Figure 26. Characteristics of the torque M as a function of time τ for $\Delta p = 10$ MPa and $n = 1500$ rpm.

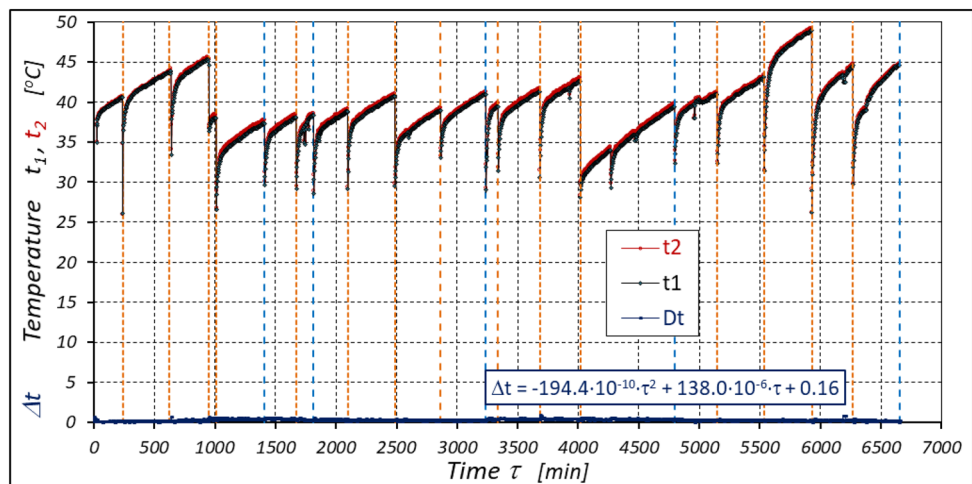


Figure 27. Characteristics of the temperatures t_1 and t_2 in the motor ports as a function of time τ for $\Delta p = 10$ MPa and $n = 1500$ rpm.

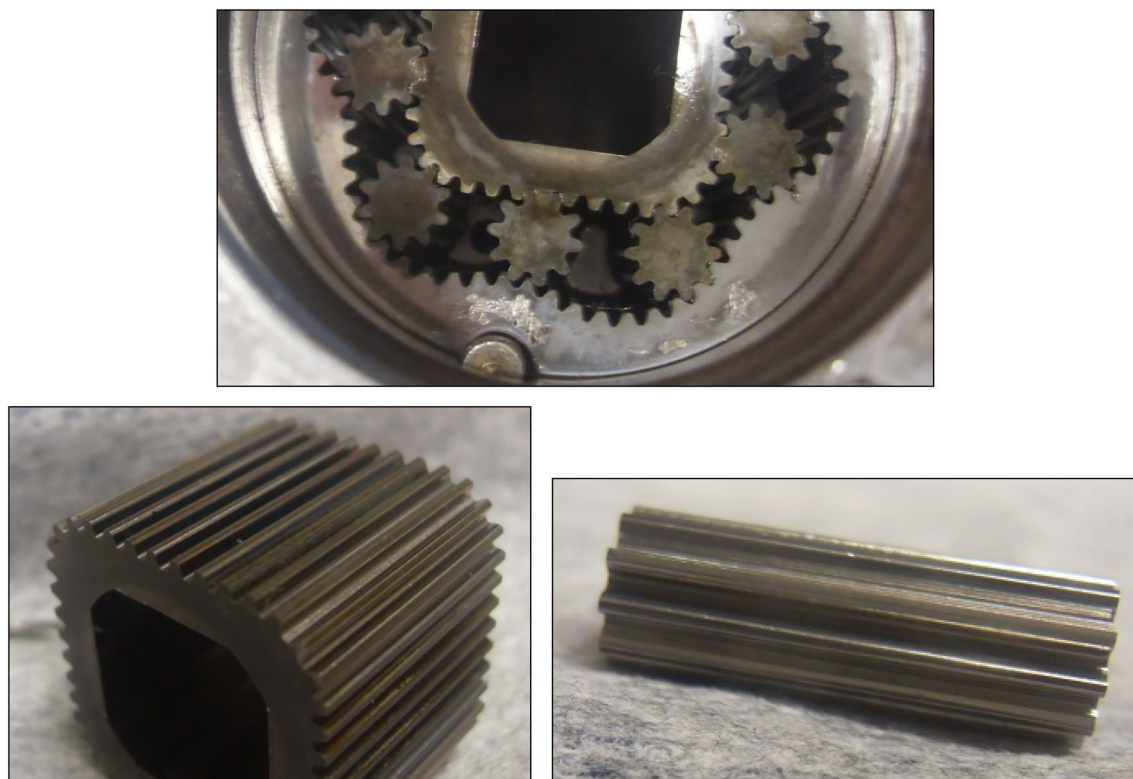


Figure 28. Satellite mechanism after the test at $\Delta p = 10$ MPa.

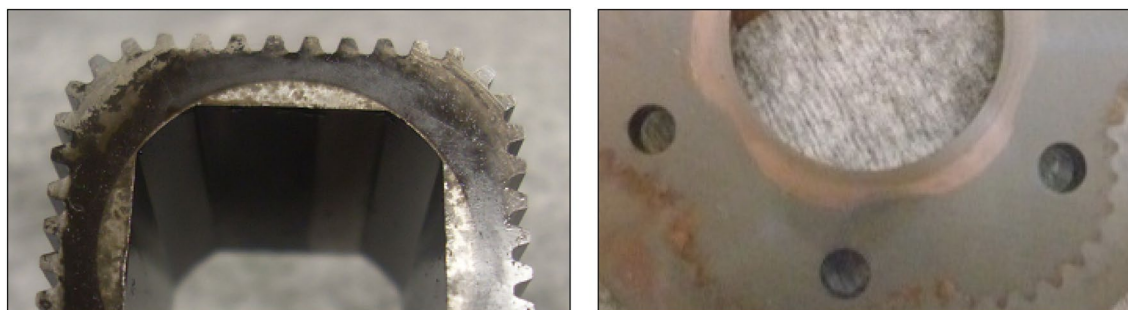


Figure 29. A layer of burnt rapeseed oil on the rotor surface (left) and the characteristic purple layer on the commutation plate (right) —after 3237 min of operation.

The result is a lower value of the torque M measured on the motor shaft (Fig. 31) and a lower mechanical-pressure efficiency η_{hm} (Fig. 33).

According to Figs. 32 and 33 the value of the volumetric efficiency η_v and the mechanical-pressure efficiency η_{hm} changes during the time τ of motor operation as follows:

a) for $\Delta p = 10$ MPa:

$$\eta_v = 0.99 + 13.55 \cdot 10^{-10} \cdot \tau^2 - 11.72 \cdot 10^{-6} \cdot \tau \quad (22)$$

$$\eta_{hm} = 0.74 - 5.92 \cdot 10^{-10} \cdot \tau^2 - 7.65 \cdot 10^{-6} \cdot \tau \quad (23)$$

b) for $\Delta p = 15$ MPa:

$$\eta_v = 0.989 - 33.08 \cdot 10^{-10} \cdot \tau^2 + 4.08 \cdot 10^{-6} \cdot \tau \quad (24)$$

$$\eta_{hm} = 0.842 - 28.75 \cdot 10^{-10} \cdot \tau^2 - 4.23 \cdot 10^{-6} \cdot \tau \quad (25)$$

c) for $\Delta p = 20$ MPa:

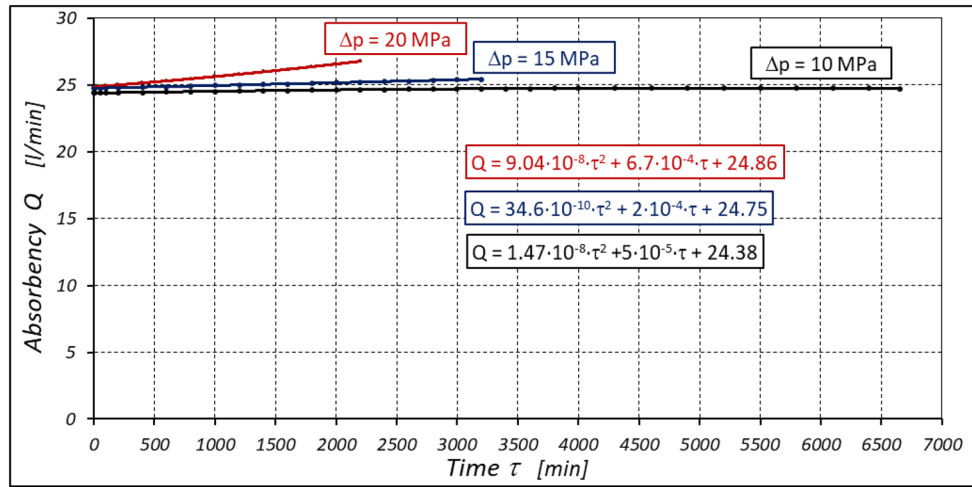


Figure 30. Characteristics of the motor absorbency Q as a function of time τ for different fixed pressure drop Δp in the motor.

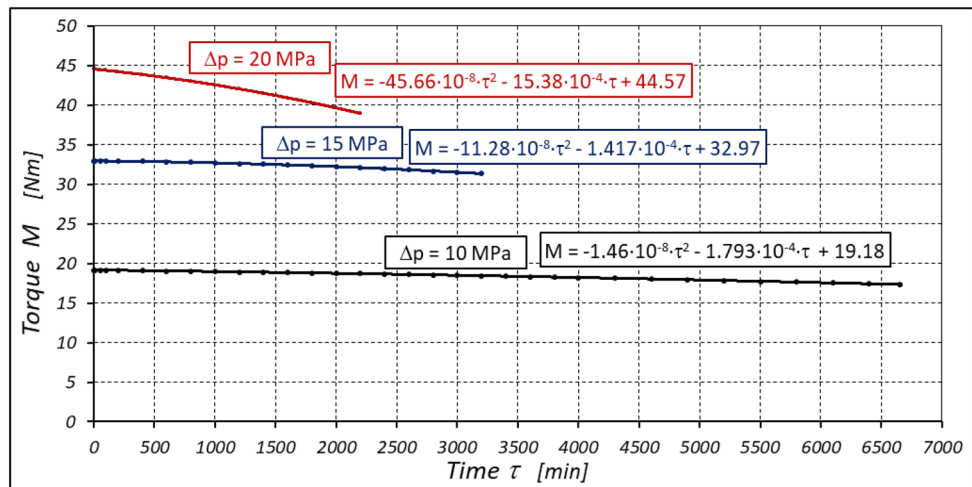


Figure 31. Characteristics of the torque M as a function of time τ for different fixed pressure drop Δp in the motor.

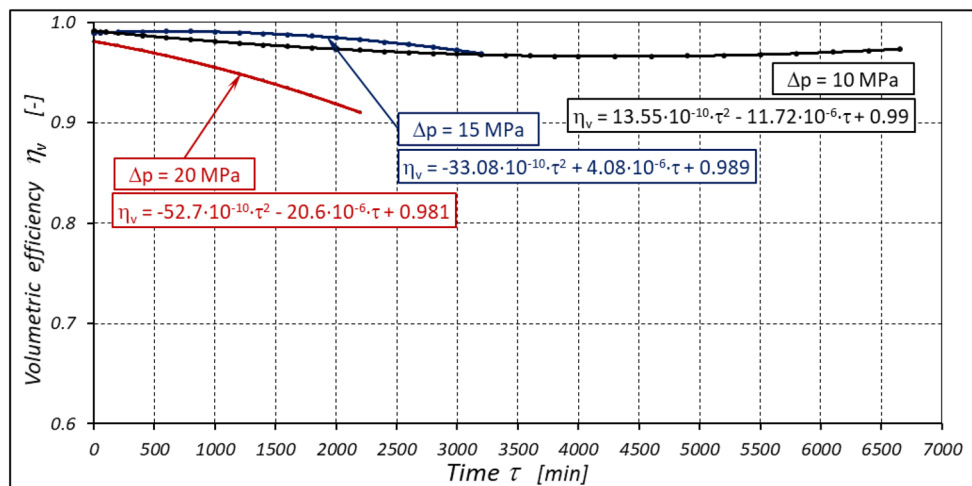


Figure 32. Volumetric efficiency η_v of the motor as a function of time τ for different fixed pressure drop Δp in the motor.

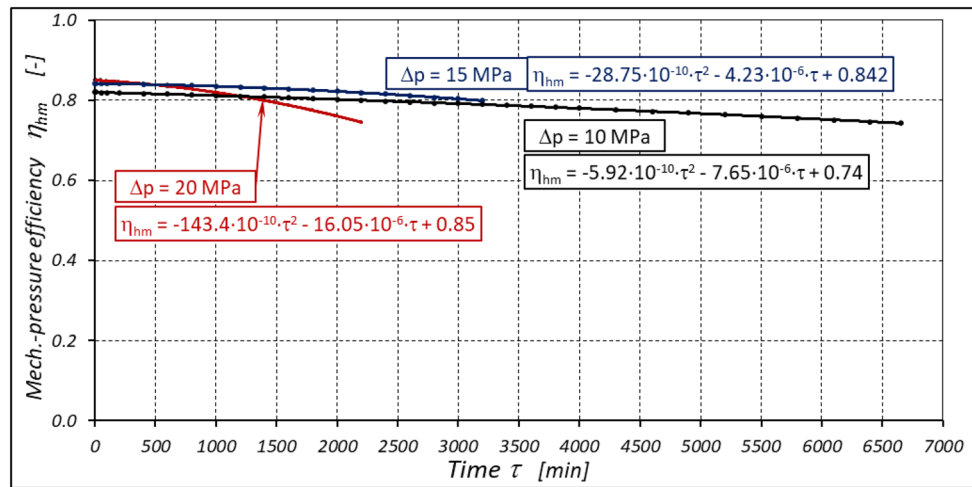


Figure 33. Mechanical-pressure efficiency η_{hm} of the motor as a function of time τ for different fixed pressure drop Δp in the motor.

$$\eta_v = 0.981 - 52.7 \cdot 10^{-10} \cdot \tau^2 - 20.6 \cdot 10^{-6} \cdot \tau \quad (26)$$

$$\eta_{hm} = 0.85 - 143.4 \cdot 10^{-10} \cdot \tau^2 - 16.05 \cdot 10^{-6} \cdot \tau \quad (27)$$

In publications^{22,37} it was shown that for the satellite motor supplied with mineral oil, in the first period of its operation (i.e. for the so-called new motor) there is:

- (a) for $\Delta p = 10$ MPa: $\eta_v = 0.96$ and $\eta_{hm} = 0.73$;
- (b) for $\Delta p = 15$ MPa: $\eta_v = 0.95$ and $\eta_{hm} = 0.82$;
- (c) for $\Delta p = 20$ MPa: $\eta_v = 0.94$ and $\eta_{hm} = 0.87$.

From the test results and the analyses described above, it can be concluded that the partial efficiencies of the satellite motor supplied with rapeseed oil are comparable to those of the motor supplied with mineral oil.

The increase in the absorbency Q of the motor and thus the decrease in the volumetric efficiency η_v over time is the result of wear processes in the working mechanism. This is shown in particular by the loss of mass of the mechanism components and the increase in the axial clearance of the rotor and satellites (Tables 3, 4 and Table 5). The characteristics of the absorbency Q and volumetric efficiency η_v of the motor at $\Delta p = 10$ MPa are quite unexpected (Figs. 30 and 32). The absorbency Q of the motor does not change much as a function of time τ (initially it increases slightly up to $t \approx 3500$ min and then decreases slightly—Fig. 30), although the axial clearances of the rotor and the satellites have increased considerably (Table 5).

It was also observed that rapeseed oil sticks to the front surface, especially the rotor (Figs. 28 and 29). Tribological examinations of the materials of the friction pairings lubricated with rapeseed oil showed that it is a film of burnt oil. This burnt oil layer is characterised by very good tribological properties^{22,45}. The thickness of this layer was measured and found to be comparable to the height of the gap between the rotor and the commutation plate. Table 5 shows quite large values for the axial clearance of the rotor and the satellites, as these are the values after running-in of the elements (as already written in Sect. 7.3) and therefore do not include a burnt oil layer.

It is significant that at higher pressure drops in the motor, i.e. at $\Delta p > 10$ MPa. This can be explained as follows. The flow in the flat gap formed by the rotor and the commutation plate is a function of the pressure drop in this gap³⁹. The flow in this gap is the flow from the HPC high pressure chamber to the shaft chamber. The shaft chamber is connected to the HPC low-pressure chamber²². Therefore, the pressure drop in this gap is comparable to the pressure drop Δp_i in the working chambers.

Therefore, at low Δp_i there is a very low value of flow in the gap. In addition, there are errors in the manufacturing of the components of the working mechanism. This means that the rotor surface is not parallel to the commutation plate and there is friction between these elements. As a result, the surface temperature of these elements increases. With a very low liquid flow in the gap, these surfaces do not have time to cool down. Therefore, the oil particles are burnt and a layer of burnt oil forms. With larger pressure drops Δp_i in the working chambers, there is a larger flow of liquid in the gap. This is sufficient to prevent an excessive rise in temperature.

The test results confirmed the theoretical analyses described in Sect. 5 regarding the temperature increase Δt in the motor. This Δt (measured in the motor ports) is the result of the energy losses occurring in the motor. Formula (14) shows that the liquid parameters that have a direct impact on the temperature increase in the motor are density ρ and specific heat c . However, the viscosity ν of the liquid has an indirect effect, i.e. it significantly affects the volumetric efficiency η_v of the motor, the pressure efficiency η_h of the motor and, to a much lesser extent, the mechanical efficiency η_m of the motor, which has been demonstrated in the author's previous publications, including: in^{22,39,40}.

The temperature difference Δt in the motor can therefore be an indicator of the total efficiency η_c . This efficiency can therefore be calculated by transforming formula (14), i.e.:

$$\eta_c = 1 - \rho \cdot c \cdot \left(k + \frac{\Delta T}{\Delta p} \right) \quad (28)$$

As there is no information in the literature regarding the value of the k constant for mineral oil, the value of this constant was calculated according to formula (16), where the efficiency values η_v and η_{hm} and rise in temperature Δt were calculated according to formulas (22) + (31). In this way, $k = 0.071 \text{ }^\circ\text{C}/\text{MPa}$ was determined. This value appears to be quite realistic. For comparison, the value k given in⁵² for Hydrol mineral oil at the same temperature is $k = 0.128 \text{ }^\circ\text{C}/\text{MPa}$. For comparison purposes, Fig. 34 shows the rise in temperature Δt in the motor, which was calculated according to formula (14) (for $k = 0.071 \text{ }^\circ\text{C}/\text{MPa}$) and obtained from the experiment.

The differences between the calculated and measured temperatures are not large. Therefore, these differences do not disqualify the tests described above. Therefore, the lower the total efficiency η_c of the motor, the greater the rise in temperature Δt in the motor. Measuring the temperature difference Δt in the motor can therefore be an indicator of the overall efficiency of the motor.

The experimental data (Figs. 14, 22 and 26) show that the rise in temperature Δt changes during the time τ of motor operation as follows:

a) for $\Delta p = 10 \text{ MPa}$:

$$\Delta t = 0.16 - 194.4 \cdot 10^{-10} \cdot \tau^2 + 138.0 \cdot 10^{-6} \cdot \tau \quad (29)$$

b) for $\Delta p = 15 \text{ MPa}$:

$$\Delta t = 0.93 + 155.7 \cdot 10^{-10} \cdot \tau^2 - 66.4 \cdot 10^{-6} \cdot \tau \quad (30)$$

c) for $\Delta p = 20 \text{ MPa}$:

$$\Delta t = 0.42 + 61.5 \cdot 10^{-10} \cdot \tau^2 + 828.6 \cdot 10^{-6} \cdot \tau \quad (31)$$

As already mentioned abrasive wear of the gear elements of the working mechanism also occurs during motor operation, resulting in weight loss of these elements. The greatest and fastest weight loss of these elements occurs at the highest motor loads (Figs. 35, 36 and 37).

Furthermore, the characteristics presented in Figs. 35, 36 and 37 show that the rotor has the greatest relative weight loss, especially at $\Delta p \geq 15 \text{ MPa}$. The reasons for this are as follows:

- (1) during one complete revolution of the rotor, each rotor tooth is loaded the greatest number of times (see Sect. 2 and³⁸);
- (2) the change in the direction of tooth loadin that occur during the phase change of the chambers adjacent to the satellite (i.e. during the transition of the chamber from the high-pressure chamber to the low-pressure chamber and vice versa);
- (3) the presence of a centrifugal force acting on the satellite. Its effect is the disappearance of the clearances in the co-operation between the satellite and the bypass and the increase in the clearances in the co-operation between the satellite and the rotor, which is shown in Figs. 28 and 38. Therefore, in the area of co-operation between the satellite teeth and the rotor teeth, the conditions for co-operation deteriorate;
- (4) within the inter-tooth clearance, there is a phenomenon of the satellite tooth hitting the rotor tooth when the pressure in the chamber changes from low to high³⁸.

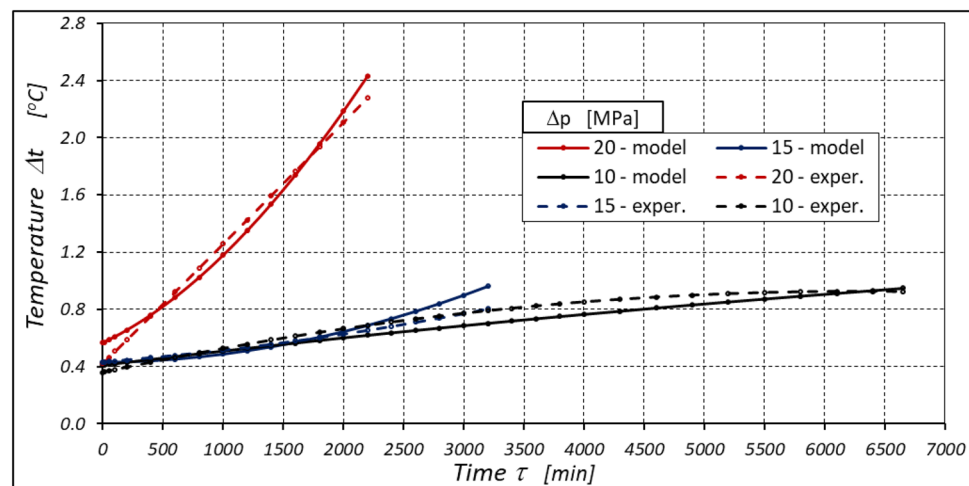


Figure 34. Rise in temperature Δt in the motor as a function of the motor operation time τ calculated according to formula (14) and the result of the experiment.

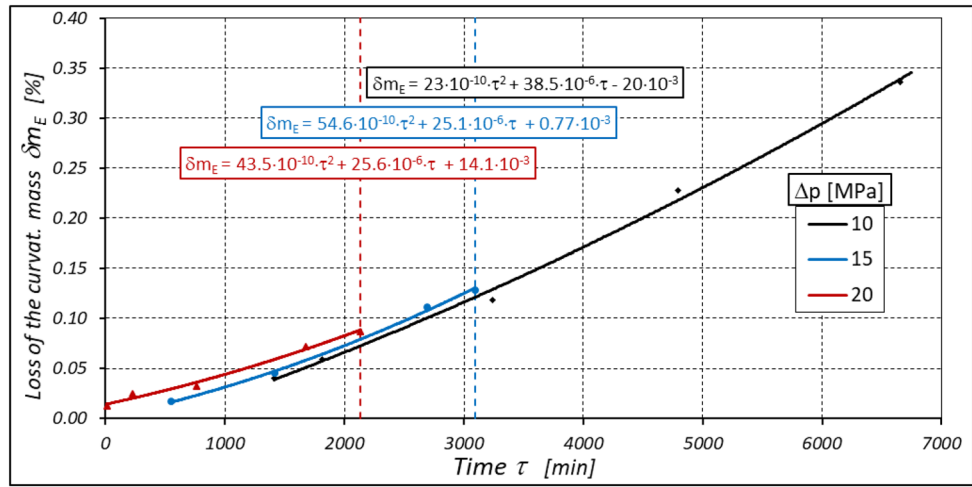


Figure 35. Percentage loss δm_E of the curvature mass as a function of time τ .

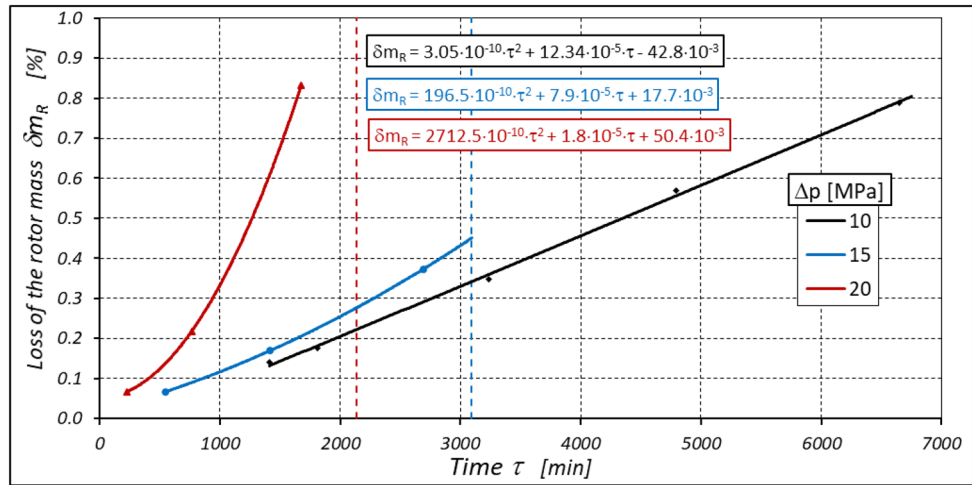


Figure 36. Percentage loss δm_R of the rotor mass as a function of time τ .

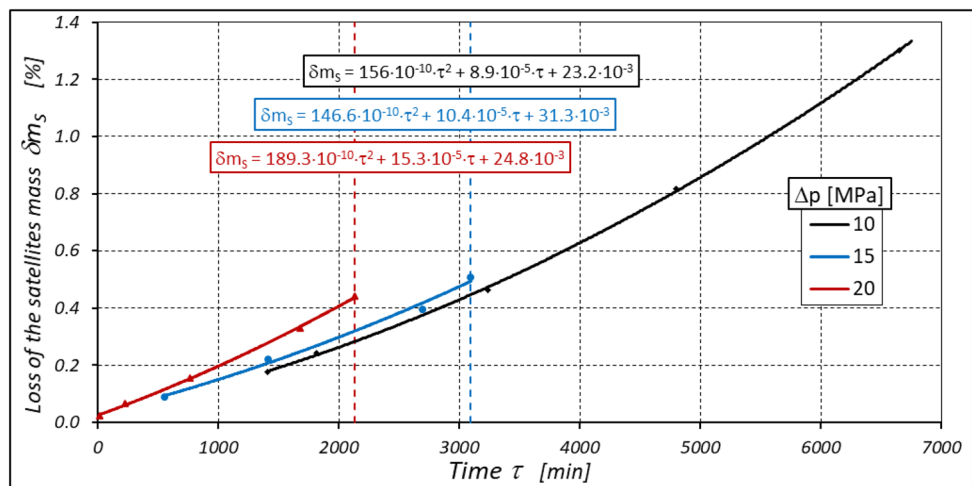


Figure 37. Percentage loss δm_S of the satellites mass as a function of time τ .

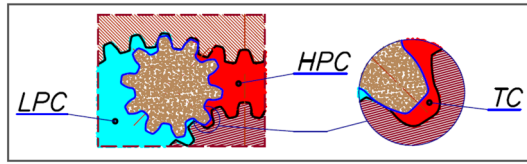


Figure 38. Unfavourable position of the satellite in relation to the rotor—large intertoothed and tip clearances of the interacting teeth.

Due to the phenomena described above, the rotor wears out the fastest. The curvature wears the slowest because it has the most favourable working conditions.

During the motor operation time τ , until the mechanism is destroyed, a certain number of load cycles occur on each curvature tooth, rotor and satellite. This number can be calculated using the following formula:

a) for the satellite tooth:

$$i_{ds} = i_s \cdot (n \cdot \tau + n_m \cdot \tau_s) \tag{32}$$

b) for the rotor tooth:

$$i_{dRTS} = i_{RTS} \cdot (n \cdot \tau + n_m \cdot \tau_s) \tag{33}$$

c) for the curvature tooth:

$$i_{dETS} = i_{ETS} \cdot (n \cdot \tau + n_m \cdot \tau_s) \tag{34}$$

where the set-up time τ_s and the mean rotational speed n_m were described in Sect. 6.

An overview of the number of cycles i_d for each element of the mechanism from all test series is shown in Table 6.

From the results in the above table, it can be concluded that:

- (a) the rotor teeth are characterised by the highest number of load cycles;
- (b) the durability of the working mechanism for $\Delta p > 10$ MPa is very low (approx. 51.5 h for $\Delta p = 15$ MPa and 35.5 h for $\Delta p = 20$ MPa);
- (c) the durability of the working mechanism cannot be accurately determined for $\Delta p = 10$ MPa, as the test was cancelled after more than 110 h of motor operation;
- (d) to achieve satisfactory durability of the satellite mechanism, the motor should be operated at $\Delta p < 10$ MPa;
- (e) the results of the theoretical analyzes contained in³⁸ were confirmed, i.e. the working mechanism is overloaded (especially at $\Delta p = 20$ MPa) and the stresses in the teeth of this mechanism exceed the permissible values.

A significant observed phenomenon in each series of tests is the increase in the height of the curvature and the increase in the axial clearance of the rotor and satellites (Tables 3, 4 and 5). It can be seen that this phenomenon correlates with the phenomenon of fretting on the end surfaces of the curvature and the commutation plates (Figs. 17, 18 and 28). The reason for this phenomenon is the low stiffness of the curvature. When the pressure drop Δp_{ich} in the working chambers increases, the actual working volume of the mechanism increases, which has been demonstrated in publications^{37,47,48}. Therefore, elastic deformation of both the curvature and the commutation plates must occur, which is evidenced by the visual effect, i.e. fretting. As a result of fretting, detached particles of the curvature material and the commutation plates can be hammered into the surface, especially of the curvature in the immediate vicinity of the fretting centre.

The curvature is an element made of a material that has a lower hardness than the commutation plate (sintered carbide). This create bumps on the curvature that increase its height. During periodic disassembly of the motor, these bumps were carefully removed by lapping. However, care was taken not to break in too intensively so as not to reduce the height of the curvature and thus not to eliminate the axial clearances of the satellites and the rotor. Therefore, these bumps were not completely removed, which led to an increase in the axial clearance.

| | τ (min) | τ_s (min) | i_s | i_{RTS} | i_{ETS} | i_{ds} | i_{dRTS} | i_{dETS} |
|------------------|--------------|----------------|-------|-----------|-----------|------------|------------|------------|
| Δp (MPa) | | | | | | | | |
| 10* | 6652* | 52 | 5.28 | 6 | 4 | 52,889,760 | 60,102,000 | 40,068,000 |
| 15 | 3092.5 | 30 | | | | 24,611,400 | 27,967,500 | 18,645,000 |
| 20 | 2135 | 40 | | | | 17,067,600 | 19,395,000 | 12,930,000 |

Table 6. The number of load cycles of the teeth until their destruction for $n = 1500$ rpm and $n_m = 750$ rpm. *The mechanism is not destroyed!

Final conclusion

The test results of a satellite motor supplied with rapeseed oil have proven that:

- (1) the satellite motor can be supplied with rapeseed oil;
- (2) the efficiencies of the tested motor are comparable to the efficiencies of the motor supplied with mineral oil;
- (3) the durability of the satellite mechanism strongly depends on the pressure drop Δp_i in the working chambers, and thus depends on the motor load M and its absorbcency Q ;
- (4) the satellite mechanism is generally characterised by very low durability at a pressure drop higher than 10 MPa. The research results confirmed the general conclusion from the theoretical analyses described in³⁸, i.e. ‘satellite positive displacement machines (pumps, motors) should operate at low speed and at most an average working pressure’;

From the research results presented in this article, it can also be concluded that it is necessary to develop a tooth profile (shape) other than that of the involute and characterised by lower stresses in the area of cooperation. This procedure would have a positive effect on extending the operating time of the satellite mechanism and thus on its durability, especially under high loads M .

Data availability

The datasets used and/or analysed during the current study are available from the corresponding author on reasonable request.

Received: 7 March 2024; Accepted: 30 April 2024

Published online: 07 May 2024

References

1. AL-Assady, A. & AL-Khafaji, M. Design and analysis of electro-hydraulic servo system for speed control of hydraulic motor. *J. Eng.* **19**(05), 562–573 (2013).
2. Bobe, A., Axinte, T., Nutu, C. S., Fratila & C., Diaconu, M.: Aspects regarding the use of hydraulic motors. *Hidraulica* **4**. https://www.researchgate.net/publication/366399771_Aspects_regarding_the_Use_of_Hydraulic_Motors#fullTextFileContent (2022).
3. Darnet, J., Bideaux, E. & Tregouet, J.: Projection Method for Hydraulic Piston Motor Torque Control. In.: Proceedings of the ASME/BATH 2023 Symposium on Fluid Power and Motion Control. ASME/BATH 2023. V001T01A02. <https://doi.org/10.1115/FPMC2023-111492> (2023).
4. Jasinski, R. Analysis of the heating process of hydraulic motors during start-up in thermal shock conditions. *Energies* **15**(1), 55. <https://doi.org/10.3390/en15010055> (2022).
5. Kiurchev, S., Kyurchev, V., Fatyeyev, A., Tynyanova, I. & Mudryk, K. Influence of the radius of curvature of the teeth on the geometric and functional parameters of the rotors of the planetary hydraulic motor. In *Advanced Manufacturing Processes V InterPartner 2023 Lecture Notes in Mechanical Engineering* (eds Tonkonogyi, V. et al.) (Springer, 2024).
6. Salam, M. A. *Hydraulic motors. Fundamentals of Pneumatics and Hydraulics* (Springer, 2022).
7. Banaszek, A. Methodology of flow rate assessment of submerged hydraulic ballast pumps on modern product and chemical tankers with use of neural network methods. *Proc. Comp. Sci.* **192**(4), 1894–1903. <https://doi.org/10.1016/j.procs.2021.08.195> (2021).
8. Petrovic, R. & Banaszek, A. Problem of non proportional flow of hydraulic pumps working with Constant pressure regulators in big power multipump power pack unit in open system. *Tech. Vjes.* **26**(2), 294–301 (2019).
9. Stosiak, M. & Karpenko, M. The influence of the hydropneumatic accumulator on the dynamic and noise of the hydrostatic drive operation. *Eksp. Niez. Maint. Rel.* **26**(2), 1–11 (2024).
10. Kollek, W. & Radziwanowska, U. Energetic efficiency of gear micropumps. *Arch. Civ. Mech. Eng.* **15**(1), 109–115. <https://doi.org/10.1016/j.acme.2014.05.005> (2015).
11. Stawinski, L., Kosucki, A., Cebulak, M., Gorniak vel Gorski, A. & Grala, M. Investigation of the influence of hydraulic oil temperature on the variable-speed pump performance. *Eksp. Niez. – Maint. Rel.* **24**(2) (2022).
12. Zaluski, P. Influence of fluid compressibility and movements of the swash plate axis of rotation on the volumetric efficiency of axial piston pumps. *Energies* **15**(1), 298. <https://doi.org/10.3390/en15010298> (2022).
13. Novak, N., Trajkovski, A., Polajnar, M., Kalin, M. & Majdic, F. Wear of hydraulic pump with real particles and medium test dust. *Wear* **532–533**, 205101. <https://doi.org/10.1016/j.wear.2023.205101> (2023).
14. Novak, N., Trajkovski, A., Kalin, M. & Majdic, F. Degradation of hydraulic system due to wear particles or medium test dust. *Appl. Sci.* **13**, 7777. <https://doi.org/10.3390/app13137777> (2023).
15. Strmcnik, E. & Majdic, F. The pressure and efficiency characteristic of hydraulic gerotor motor with the floating outer ring. *Tech. Vjes.* **25**(2), 609–615 (2018).
16. Majdic, F., Kalin, M. & Pezdirnik, J. In: *Proceedings of the JFPS International Symposium on Fluid Power. An analytical comparison of hydraulic systems based on water and on oil.* TOYAMA 2008. <https://doi.org/10.5739/isfp.2008.679> (2008).
17. Osinski, P., Deptula, A. & Partyka, M. Hydraulic tests of the PZ0 gear micropump and the importance rank of its design and operating parameters. *Energies* **15**(9), 3068. <https://doi.org/10.3390/en15093068> (2022).
18. Cieslikowski B. & Slipek Z.: Zmienność cech oleju rzepakowego w warunkach przechowywania (Variance of rape oil qualities under storage conditions). *Inż. Rol.* **13**. https://ir.ptir.org/artykuly/pl/88/IR%2888%29_418_pl.pdf (2006).
19. Drabik J.: Ocena odporności na utlenianie oraz właściwości smarnych kompozycji oleju roślinnego (The assessment of oxidation stability and of lubricating properties of vegetable oil compositions). *Trib.* **3**. <https://t.tribologia.eu/resources/html/article/details?id=165245&language=pl> (2009).
20. Rogos E. & Urbanski A.: Biodegradowalny olej hydrauliczny o podwyższonych właściwościach smarnych (Biodegradable hydraulic oil with improved lubricating properties). *Trib.* **2**. <https://t.tribologia.eu/resources/html/article/details?id=165886> (2009).
21. Rudko, T. & Rybczynski, R. Właściwości smarne olejów roślinnych i mineralnych stosowanych w układach tnących pilarek (Lubrication properties of vegetable and mineral oils used for cutting mechanism of chainsaws). *Acta Agr.* **15**(1), 177 (2010).
22. Sliwinski, P. *Satelitowe maszyny wporowe. Podstawy projektowania i Analiza strat energetycznych (Satellite displacement machines Basic of design and analysis of power loss)* (Gdansk University of Technology Publishers, 2016).
23. Kujawski, M. *Mechanizmy obiegowe z nieokrągłymi kołami zębatymi, podstawy projektowania i wykonania (Circulation mechanisms with non-circular gears: the basics of design and manufacturing)*. Poznan University of Technology Publishing House (1992).

24. Sliwinski, P. The methodology of design of satellite working mechanism of positive displacement machine. *Sci. Rep.* **12**, 13685. <https://doi.org/10.1038/s41598-022-18093-z> (2022).
25. Sliwinski, P.: Mechanizm satelitowy hydraulicznej maszyny wyporowej (Satellite operating mechanism of a hydraulic displacement machine). Patent application P.445212 (2023).
26. Sliwinski, P.: Mechanizm satelitowy hydraulicznej maszyny wyporowej (Satellite operating mechanism of a hydraulic displacement machine). Patent application P.437751. <https://ewyszukiwarka.pue.uprp.gov.pl/search/pwp-details/P.437751> (2021).
27. Sliwinski, P. & Patrosz, P. Satelitowy mechanizm roboczy hydraulicznej maszyny wyporowej (eng. Satellite operating mechanism of the hydraulic displacement machine). Patent PL 218888. <https://ewyszukiwarka.pue.uprp.gov.pl/search/pwp-details/P.401821> (2015).
28. Sieniawski, B. & Skorynkiewicz S.: Silnik hydrauliczny obiegowo-krzywkowy (Hydraulic planetary gear motor). Patent PL 212435. <https://ewyszukiwarka.pue.uprp.gov.pl/search/pwp-details/P.385828> (2012).
29. Sieniawski, B. Satelitowa maszyna wyporowa (eng. Satellite displacement machine). Patent PL 216648. <https://ewyszukiwarka.pue.uprp.gov.pl/search/pwp-details/P.391060> (2010).
30. Li, D., Liu, Y., Gong, J. & Wang, T. Design of a noncircular planetary gear mechanism for hydraulic motor. *Mat. Prob. Eng.* **2021**, 5510521. <https://doi.org/10.1155/2021/5510521> (2021).
31. Zhang, B., Song, S., Jing, C. & Xiang, D. Displacement prediction and optimization of a non-circular planetary gear hydraulic motor. *Adv. Mech. Eng.* **13**, 16878140211062690 (2021).
32. Luan, Z. & Ding, M. Research on non-circular planetary gear pump. *Adv. Mat. Res.* **339**, 140–143. <https://doi.org/10.4028/www.scientific.net/AMR.339.140> (2011).
33. Volkov, G. & Fadyushin, D. Improvement of the method of geometric design of gear segments of a planetary rotary hydraulic machine. *IOP Conf. Series: J. Phys.* **1889**, 042052. <https://doi.org/10.1088/1742-6596/1889/4/042052> (2021).
34. Osiecki, L. New generation of the satellite hydraulic pumps. *J. Mech. En. Eng.* **4**. <https://doi.org/10.30464/jmee.2019.3.4.309> (2019).
35. Catalog of satellite motors of SM-Hydro company, Accessed on 19 Dec 2023. <https://smhydro.com.pl>
36. Catalog of satellite motors of PONAR company, Accessed on 19 Dec 2023. <https://www.ponar-wadowice.pl/en/type/673-motors-hydraulic-motors-satellite-hydraulic-motor-psm>
37. Sliwinski, P. The influence of pressure drop on the working volume of a hydraulic motor. *Eks. Niez. Main. Rel.* <https://doi.org/10.17531/ein.2022.4.15> (2022).
38. Sliwinski, P. Influence of geometrical and operational parameters on tooth wear in the working mechanism of a satellite motor. *Sci. Rep.* **13**, 17028 (2023).
39. Sliwinski, P. The influence of water and mineral oil on volumetric losses in hydraulic motor. *Pol. Mar. Res.* <https://doi.org/10.1515/pomr-2017-0041> (2017).
40. Sliwinski, P. The influence of water and mineral oil on mechanical losses in a hydraulic motor for offshore and marine application. *Pol. Mar. Res.* **27**(2), 125–135 (2020).
41. Ostrowski M. *Badania trwałościowe silnika satelitowego i gerotorowego (Research of durability n orbital and satellite gear motor)*. Master's Thesis. Gdansk University of Technology (2023).
42. Sliwinski, P. Satellite pump and motor. *Mach. Tech. Mat.* **9**(8), 8–11 (2014).
43. Panchenko, A., Voloshina, A., Antoshchenkov, R., Halych, I. & Glowacki, S. Experimental studies of the wear on the rotors' working surfaces of a planetary hydraulic motor. In *Advanced Manufacturing Processes V InterPartner 2023 Lecture Notes in Mechanical Engineering* (eds Tonkonogyi, V. et al.) (Springer, Cham, 2023).
44. Voloshina, A., Panchenko, A., Titova, O., Milaeva, I. & Pastushenko, A. Prediction of changes in the output characteristics of the planetary hydraulic motor. In: Tonkonogyi, V., et al. *Advanced Manufacturing Processes II. InterPartner 2020*. Lecture Notes in Mechanical Engineering. Springer, Cham. https://doi.org/10.1007/978-3-030-68014-5_72 (2021).
45. Lubinski, J. & Sliwinski, P. Multi parameter sliding test result evaluation for the selection of material pair for wear resistant components of a hydraulic motor dedicated for use with environmentally friendly working fluids. *Sol. St. Phen.* **225**, 115–122. <https://doi.org/10.4028/www.scientific.net/SSP.225.115> (2015).
46. Szkodo, M., Stanisławska, A. & Sliwinski, P. On the durability of the hydraulic satellite motor working mechanism in overload condition. *Adv. Mat. Sci.* **16**(1), 35–46. <https://doi.org/10.1515/adms-2016-0004> (2016).
47. Sliwinski, P. Determination of the theoretical and actual working volume of a hydraulic motor. *Energies* **13**(22), 5933. <https://doi.org/10.3390/en13225933> (2020).
48. Sliwinski, P. Determination of the theoretical and actual working volume of a hydraulic motor – Part II (The method based on the characteristics of effective absorbency of the motor). *Energies* **14**(6), 1648. <https://doi.org/10.3390/en14061648> (2021).
49. Sliwinski, P. & Patrosz, P. Methods of determining pressure drop in internal channels of a hydraulic motor. *Energies* **14**(18), 5669. <https://doi.org/10.3390/en14185669> (2021).
50. Catalog of steel NIMAX, <https://www.uddeholm.com/poland/pl/products/uddeholm-nimax/>.
51. Osiecki, A.: *Hydrostatyczny napęd maszyn*. WNT Warszawa (2021).
52. Balawender, A.: *Analiza energetyczna i metodyka badań silników hydraulicznych wolnoobrotowych (Energy analysis and methods of testing of low-speed hydraulic motors)*. Scientific book of the Gdansk University of Technology, Mechanika No. 54. Gdansk University of Technology Publishing House (1988).

Acknowledgements

Many thanks to Marcin Ostrowski (M.Sc., Eng.), for his invaluable help in the laboratory with the acquisition of experimental data.

Author contributions

The manuscript was written entirely by Pawel Sliwinski.

Competing interests

The authors declare no competing interests.

Additional information

Correspondence and requests for materials should be addressed to P.S.

Reprints and permissions information is available at www.nature.com/reprints.

Publisher's note Springer Nature remains neutral with regard to jurisdictional claims in published maps and institutional affiliations.



Open Access This article is licensed under a Creative Commons Attribution 4.0 International License, which permits use, sharing, adaptation, distribution and reproduction in any medium or format, as long as you give appropriate credit to the original author(s) and the source, provide a link to the Creative Commons licence, and indicate if changes were made. The images or other third party material in this article are included in the article's Creative Commons licence, unless indicated otherwise in a credit line to the material. If material is not included in the article's Creative Commons licence and your intended use is not permitted by statutory regulation or exceeds the permitted use, you will need to obtain permission directly from the copyright holder. To view a copy of this licence, visit <http://creativecommons.org/licenses/by/4.0/>.

© The Author(s) 2024